



UNIVERSITÀ DEGLI STUDI DI MILANO

Facoltà di Scienze e Tecnologie

Laurea Triennale in Fisica

**Structure, Energetics,
and Dynamic Properties
of a Colloidal Monolayer
on a Quasiperiodic
Potential Substrate**

Relatore: Prof. Nicola Manini

Correlatore: Dott. Andrea Vanossi

Dario Bertazioli
Matricola n° 851656
A.A. 2017/2018

Codice PACS: 61.44.Br

Structure, Energetics, and Dynamic Properties of a Colloidal Monolayer on a Quasiperiodic Potential Substrate

Dario Bertazioli

Dipartimento di Fisica, Università degli Studi di Milano,
Via Celoria 16, 20133 Milano, Italia

December 14, 2018

Abstract

We investigate the static and dynamic properties of a monolayer of mutually repulsive colloidal particles interacting with an externally imposed quasiperiodic corrugation potential. Using classical molecular dynamics we simulate an annealing process in order to generate a minimum total-energy configuration. We study its static properties, including energetics and static structure factors, as a function of the corrugation amplitude. We then proceed to investigate the dynamics of this model under the action of a uniform driving force increased in small steps, in order to estimate the static-friction threshold. If this static friction is nonzero, we define such state as “pinned”. When, in contrast, the colloids slide regardless of how small the applied force is, we have an “unpinned” or “superlubric” state. We investigate at two different corrugation characteristic spacings the pinned-unpinned Aubry-type transition as the corrugation amplitude is varied. Interestingly, early depinning stages occur non uniformly, with narrow advancing stripes and broad static sections.

Advisor: *Prof. Nicola Manini*
Co-Advisor: *Dott. Andrea Vanossi*

Contents

1	Introduction	3
1.1	Lubricity in Quasicrystals	4
1.2	The Aubry Transition	4
2	The Model	5
2.1	Interactions	5
2.2	Initial Condition and Mismatch	8
2.3	The Supercell	8
3	Technical Implementation	9
3.1	Static Simulations	9
3.2	Dynamic Simulations	13
4	Static Equilibrium Properties	14
4.1	Local Properties	14
4.2	Global Structural Properties	18
5	Dynamic Properties	20
5.1	The Mobility	22
5.1.1	The Overdense Case $a_{pot} = 8.8 \mu\text{m}$	22
5.1.2	The Underdense Case $a_{pot} = 5 \mu\text{m}$	25
5.2	The Depinning Thresholds	28
5.3	Structural Properties	28
6	Discussion and Conclusion	29
	References	38

1 Introduction

Order is present everywhere in the universe: we find order in the arrangement of matter, in energy flow patterns, in a great number of works of Nature interweaving space and time. In this work, we deal with a special kind of order known as quasiperiodic order. Quasiperiodic order is an example of aperiodic order, i.e. order without periodicity. Aperiodic order has (of course) nothing to do with disorder in any of its forms. Aperiodic ordered matter shows long-range organization through space, in the same way periodic order does. The long-range organization is the main difference from amorphous matter, the latter typically showing short-range correlations only. Certain aperiodic configurations of atoms, called “quasiperiodic crystals” or “quasicrystals”, have the property to produce sharp X-ray or electron diffraction figures with discrete Bragg spots, like periodic arrays of atoms. Quasicrystals, whose discovery earned Dan Shechtman a Nobel Prize in chemistry, are a natural extension of the periodic crystal. The diffraction patterns of quasicrystals are very interesting, unveiling the existence of unexpected partial symmetries which endow them with an impressive esthetical appeal. We will see examples of those patterns in the Section related to the structural properties of our systems. Related to their non-trivial structural properties, quasicrystals are known to exhibit low sliding friction [1].

Starting from such considerations, and inspired by recent experiments and simulations [2, 3, 4] the context of our work is clear: we study a specific system, composed of a 2-dimensional layer of reciprocally repulsive colloidal particles interacting with a -importantly- quasiperiodic five-fold symmetric external potential. The model is described in Sect. 2.

Using molecular dynamics (MD) we simulate how the coupling inter-particle repulsive interactions and those between the particles and the external potential guide the system (through an annealing process reported in Sect. 3) toward the (at least local) minimum of the total energy. After a stable low-energy state is obtained, we study its structural properties and its energetics in Sect. 4. Then we apply a uniform driving constant force to all colloidal particles: this allows us to investigate the characteristics of the monolayer motions (dynamic properties discussed in Sect. 5). In particular, we can vary (typically increasing) the applied force in little “adiabatic” steps, in order to identify the static-friction threshold, if any. This method also gives (rudimentary) insight in the phenomenon of the Aubry-type transition from a low-corrugation zero-static friction sliding state to a larger corrugation regular state characterized by a finite friction force.

1.1 Lubricity in Quasicrystals

In tribology, the branch of physics studying friction and adhesion phenomena, scientists are usually interested in periodic solid incommensurate interfaces, where the crystal unit cells in front of each other are not compatible (mismatched) in their size, or angle or both, so that they cannot fit in a common unit cell of any finite size. In the reality of the macroscopic world, it is rare to observe a perfectly incommensurate interface, due to the presence of defects, irregularities, and long-range elasticity [5], but in nanotribology we can find well-defined realizations of incommensurate crystal interfaces such as colloid monolayers in an optical lattice (generated by the interference of laser beams). The same considerations and in particular the terminology developed for ordinary crystals can also be extended to quasicrystals: of course, because of the lack of periodicity, one is most likely to find an incommensurate contact between two quasicrystals, or between a crystal and a quasicrystal. This is one of the reasons why it is quite interesting to study the tribological behaviour of quasicrystals, as they are “naturally” associated to low static friction between interfaces.

1.2 The Aubry Transition

In our system, as we will see in greater detail later, we study the interaction between a colloidal monolayer laying over a quasiperiodic potential substrate. In ordinary periodic systems, when the equilibrium spacing of the mutually interacting colloids is incommensurate to the periodicity of the potential, the system is expected to show an Aubry-type [6, 7] transition from a superlubric behaviour, where there is the evidence of almost free-sliding just applying an arbitrarily small force, to a static-friction behaviour, where a finite threshold prevents the system to slide when the applied driving force is too small.

A state with the former property is commonly referred to as an “unpinned” or “superlubric” state: its “free”-sliding character is a result of a dominant role of the mutual interactions among colloids, which makes the interaction with the potential substrate almost negligible, because of the small amplitude of the potential and due to an effective mechanism of compensations of forces while the crystal is sliding, due to the incommensurate interface: a intuitive view of this process is that for every particle experiencing a braking force due to climbing out of a well of the substrate landscape, there will always be another particle, somewhere else in the (ideally infinite) layer, descending into an equivalent potential-energy well. The resulting forward force will compensate the breaking one, producing an exact force balance, thus no net friction. To achieve this state of sliding one needs to have very small or no deformation at all of the original lattice, which

slides over the corrugation as a very stiff solid.

A state with finite friction can be called “pinned”: here the interaction with the substrate is stronger, as it plays an important role in deforming the original lattice, so that the adhesion with the under-layer is so important that no sliding occurs after the applied force is too small.

In our simulative work, as well as in the experimental practice, the Aubry transition can typically occur as we increase the corrugation-amplitude of the potential substrate, modifying step by step the relative importance of both the two interactions. In solid-on-solid sliding the effective corrugation amplitude can be increased e.g. by increasing the perpendicular load applied to the interface. The existence and nature of such transition in 1 dimension [8] is well known and studied in great depth, whereas in 2 dimensions (even for periodic corrugations) the panorama is being currently investigated [9, 10], and the situation was almost unknown for quasiperiodic potentials, being explored by recent works only [11, 12, 13, 14].

2 The Model

Our system is a monolayer of charged colloidal particles immersed in a liquid solution. They can be regarded as classical point-like objects which move across a quasiperiodic external corrugation potential, represented in Fig. 1.

We identify three main interactions: one of the colloidal monolayer with the optical corrugation potential, the reciprocal repulsion among colloids, and a viscous interaction with the solution.

2.1 Interactions

We sum up our model with the equation of motion for the i -th particle, which reads:

$$m\ddot{\mathbf{r}}_i + m\eta(\dot{\mathbf{r}}_i - v_d\hat{\mathbf{x}}) = -\nabla_{\mathbf{r}_i}(U_{2-body} + U_{ext}) + \xi_i. \quad (1)$$

Here \mathbf{r}_i is the 2-dimensional vector representing the particle displacement relative to the center of the simulation cell, $\mathbf{v}_d = v_d\hat{\mathbf{x}}$ is the drift velocity of the fluid, which can be used to generate a uniform Stokes driving force $\mathbf{F} = F\hat{\mathbf{x}} = m\eta\mathbf{v}_d$ acting on the colloidal particles (ηm is the viscosity coefficient of the colloids in the fluid). ξ_i is a stochastic Gaussian random variable, introduced to take non zero-temperature effects into account. Thus ξ_i is relevant for finite temperature simulations only. Compared to the experimental value of η , our adopted value ($\eta \simeq 3.42 \text{ (ms)}^{-1}$) is smaller by a factor $\simeq 1000$, due to computational time

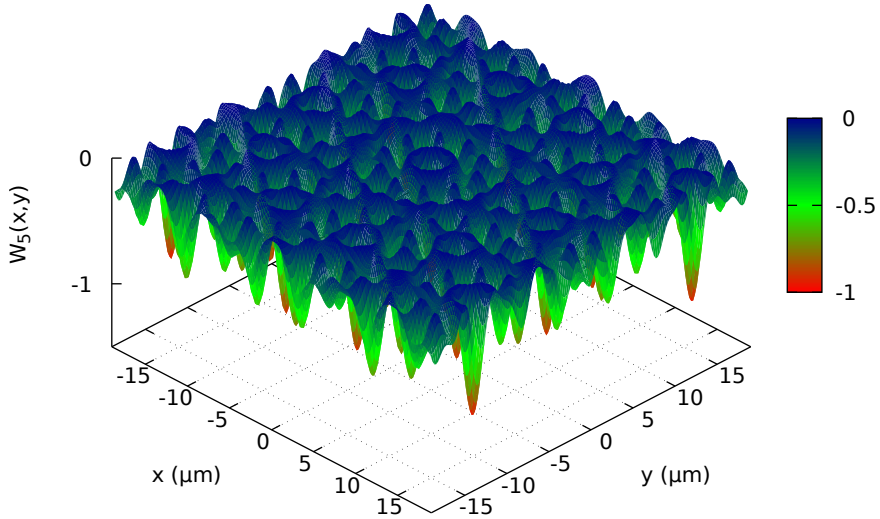


Figure 1: An example of the 5-fold symmetry external potential $W(\mathbf{r})$ representing corrugation as a function of position. Here the length scale is $a_{pot} = 5 \mu\text{m}$, and the amplitude $V_0 = 1 \text{ zJ}$. If different values of a_{pot} are considered, the function is equally stretched horizontally along x and y . When instead the corrugation amplitude V_0 is varied, it stretches along the z -axis. The optical potential exhibit recurrent patterns but no proper periodicity can be identified: thus we observe pentagonal and decagonal figures all over its extension, with no identical repetitions.

convenience: nevertheless it is still a considerably “large” value, so that the dynamics of the system is, as in the experiments, highly overdamped. This means that inertial effects play no role. Each particle’s velocity becomes proportional to the total force acting on it after a very short time of the order of η^{-1} . To better explain this fact, we consider a simplified motion equation (omitting all interactions)

$$m\ddot{\mathbf{r}} + m\eta\dot{\mathbf{r}} = 0 , \quad (2)$$

having the simple solution

$$\dot{\mathbf{r}}(t) = \dot{\mathbf{r}}_0 e^{-\eta t} , \quad (3)$$

meaning that after a time $t = \eta^{-1}$ the system loses a significant fraction of the kinetic energy by dissipating it into the solution bath.

Note however that, despite the local dynamics being accelerated by the reduced value of η , long correlation effects occur over a real time scale, because such effects are dependent on the action performed by the potential interactions (having their own time scales) rather than on the viscous dynamics. As a conse-

quence, interpreting the reduced damping purely as a “time acceleration” is not completely rigorous.

Let us now discuss the potential terms. U_{2-body} represents the 2-body mutual interaction of the colloidal particles:

$$U_{2-body} = \sum_{i < i'}^N V(|\mathbf{r}_i - \mathbf{r}_j|) . \quad (4)$$

We model the pair repulsion $V(r_{ij})$ as a Yukawa potential:

$$V(r_{ij}) = \frac{Q}{r_{ij}} e^{-\frac{r_{ij}}{\lambda_D}} . \quad (5)$$

In our simulations we take the following values for the parameters $Q = 1 \times 10^{11}$ zJ μm and $\lambda_D = 0.2 \mu\text{m}$ in order to reproduce the experimental conditions, following Refs. [9, 15, 16].

The interaction with the substrate potential is described by the one-body potential energy

$$U_{ext} = V_0 \sum_i^N W_n(\mathbf{r}_i) . \quad (6)$$

We will refer to V_0 as the corrugation-potential amplitude parameter.

The external potential is generated by the interference of laser beams, so that to describe the interference pattern created by n laser fields we use the function:

$$W_n(\mathbf{r}) = -\frac{1}{n^2} \left| \sum_{l=0}^{n-1} \exp(i\mathbf{k}_l \cdot \mathbf{r}) \right| , \quad (7)$$

where, in order to reproduce the correct (2D) interference pattern we take

$$\mathbf{k}_l = \frac{c_n \pi}{a_{pot}} \left[\cos\left(\frac{2\pi l}{n} + \alpha_n\right), \sin\left(\frac{2\pi l}{n} + \alpha_n\right) \right] . \quad (8)$$

In this equation (8) the constant c_n is introduced in order to match the lattice spacing to the laser interference periodicity a_{pot} , and α_n is chosen so that one of the main-symmetry direction of the potential $W_n(\mathbf{r})$ is directed along the x axis.

In particular, in our case we consider a pattern generated by $n = 5$ laser beams (i.e. a five-fold quasiperiodic potential) and consequently we adopt the following values for the constants above: $c_5 = 2$ and $\alpha_5 = 0$ [3].

The present definition of $W_5(\mathbf{r})$ matches that defined in Ref. [17], and in particular the typical corrugation length scale a_{pot} coincides with a_v in that paper.

2.2 Initial Condition and Mismatch

In our simulations for the initial state of the colloids we take an hexagonal lattice with fixed spacing $a_{coll} = 5.8 \mu\text{m}$ corresponding to a density $\simeq 0.0343 \text{ colloids } (\mu\text{m})^{-2}$. At this spacing, the nearest-neighbours repulsive energy is $V(5.8 \mu\text{m}) \approx 0.0044 \text{ zJ}$, and the nearest-neighbours repulsive force $-V'(5.8 \mu\text{m}) \approx 0.0227 \text{ fN}$.

For this fixed density, we study two situations characterized by the following values of the external potential length scale $a_{pot} = 8.8 \mu\text{m}$ and $a_{pot} = 5 \mu\text{m}$. Those values are chosen in order to explore rather "extreme" points of the possible system arrangements: indeed the former case tends to be an "overdense" configuration, where the ratio $\frac{a_{pot}}{a_{coll}} > 1$ indicates that more than one colloidal particle is available to fill each potential well, whereas the latter situation can be considered as an "underdense" case, with the ratio $\frac{a_{pot}}{a_{coll}} < 1$ indicating fewer particles than deep potential wells.

2.3 The Supercell

We need to maintain a fixed and well-defined average density of colloids against their mutual repulsion. This could be achieved with a rigid boundary confining colloids in a given area. To better simulate a much larger (ideally infinite) region, we rather implement periodic boundaries. Thus the colloidal system is simulated in a supercell which allows us to fix the density as the total particle number N divided by the supercell area, while allowing particles in and out this area, e.g. when sliding. To prevent problems at the boundary, the horizontal length of the cell side is taken as a multiple L of the lattice spacing a_{coll} . For the other (y) direction we also need to satisfy the boundary conditions for the hexagonal lattice (of colloids). To take the supercell as square as possible we adopt a rectangle $L \times L' = 100a_{coll} \times 58\sqrt{3}a_{coll} = 580\sqrt{3}a_{coll}^2 \simeq 337943 \mu\text{m}^2$. With the given a_{coll} , this supercell fits $N = 11600$ colloids, corresponding to a density $\rho = N/A \simeq 0.0343 \text{ } (\mu\text{m})^{-2}$.

If the substrate potential was periodic, we could have chosen proper supercell vectors in order to fullfil both the periodic boundary conditions (PBC) of the hexagonal lattice and the external potential lattice [15]: however, the potential being quasiperiodic, it is impossible to implement any exact PBC compatible with $W(\mathbf{r})$. We will prove later that the mismatch between the PBC and our potential will not be pathologic, in particular if we neglect a small region near the boundary where boundary-effects may arise.

Physical quantity	model notation	value
potential characteristic spacing	a_{pot}	8.8 μm or 5 μm
colloidal lattice spacing	a_{coll}	5.8 μm
supercell sides	$L \times L'$	580 $\mu\text{m} \times 336.4\sqrt{3} \mu\text{m}$
number of colloids	N	11600
colloidal layer mass	m	31.0593557697 fkg
damping rate	η	3.425150 $(\text{ms})^{-1}$
Yukawa potential strength	Q	$1 \times 10^{11} \text{ zJ} \times \mu\text{m}$
Debye screening length	λ_d	0.2 μm

Table 1: Simulation parameters used in our model.

Table 1 collects the simulation parameters used in this work.

3 Technical Implementation

3.1 Static Simulations

We first of all need to recover a stable state of minimum (total) energy for the system. An example of such minimum-energy configuration can be achieved by means of a simulated relaxation, where the system go toward a minimum state for which indeed the potential energy is minimized, at least locally. During this relaxation, a compromise is found in the competition (called *length-scale competition* [18]) between the external-potential corrugation, which would tend to fit as many particles as possible in the deepest potential wells, see Fig. 1, and the other main interaction, the mutual repulsion among particles, which tends to maintain the colloidal lattice close to its initial hexagonal lattice which is optimal for the repulsive inter-particle interaction.

The resulting “just damped” state is certainly a local minimum, but it is not necessarily the best one. Starting from this configuration, we try to improve it by means of a simulated annealing process: we increase the temperature of our system from the initial null value used for the first relaxation, up to a suitable value T_{start} adapted to each different corrugation potential, as listed in Table 2. This higher temperature helps the system to explore several available configurations by giving the particles the possibility of climbing over potential barriers thanks to the thermal random forces.

We then perform a sequence of simulations decreasing the temperature in small steps. We use the final configuration of each simulation as the starting

a_{pot} (μm)	V_0 (zJ)	T_{start} (zJ)
8.8	0.1	0.003
	0.2	0.05
	0.5	0.1
	0.8	1
	1	1
	5	1.08
	10	2.24
	30	7
	50	12.8
5	0.1	0.003
	0.2	0.05
	1	1
	5	1.3
	10	2.6
	30	8
	50	14.4

Table 2: The initial temperature (T_{start}) of the annealing process for each value of the characteristic spacing a_{pot} and the corrugation amplitude V_0 . Temperature ($k_b T$, actually) is measured in zJ. For comparison, in these units room temperature 300 K corresponds to 4.14 zJ.

point for the next one, until the eventual $T = 0$ zJ value is reached again. The last step, at $T = 0$ zJ, is carried out until the system reaches a total kinetic energy $E_{kin} < 10^{-15}$ zJ for two consecutive iterations. This annealing process is summarized in Fig. 2, comparing the potential energy lowering obtained in the simple damping to the successive annealing steps, which in this, and in most cases, lead to a final configuration characterized by a significantly lower energy.

We observe that for sizeable values of the potential amplitude ($V_0 > 1$ zJ) this last step at $T = 0$ zJ is relatively fast¹, i.e. soon after cooling down to zero temperature the system collapses into a local minimum, whereas for smaller V_0 the system requires much longer time to reach a stable low-energy configuration.

The extreme example of this situation is the state corresponding to the small V_0 value ($V_0 = 0.1$ zJ for both the a_{pot} spacings): in this case the annealing process at $T_{start} = 0.002$ zJ leads to exactly the same total energy of the just damped

¹Usually requiring a simulation time $t \div 10^3\text{-}10^4\mu\text{s}$, whereas smaller corrugations require usually $t \div 10^5\text{-}10^7\mu\text{s}$.

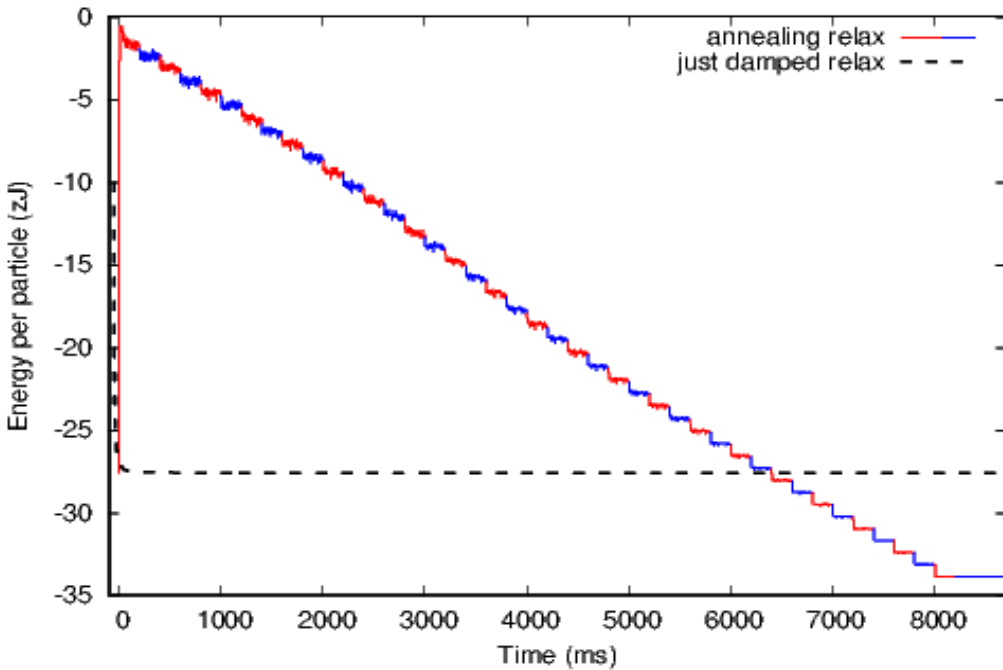


Figure 2: Example of total energy evolution resulting from a typical relaxation simulation (dashed line) and from a successive annealing (solid lines). Here $a_{pot} = 5 \mu\text{m}$, $V_0 = 50 \text{ zJ}$. The starting point of the relaxation simulation is the hexagonal colloidal lattice state, whereas the annealing cycle starts from the final configuration of the first relaxation, thus the solid line starts at the same energy level as the dashed-line end point. The final configuration achieved at the end of the annealing process is significantly lower in energy than the just-damped one.

relaxation. Annealings to higher temperatures lead to worst configurations. This suggests that for such small value of V_0 the role played by the potential itself is so much less important than the dominant role played by the colloidal interaction, which tends to maintain the overall structure very close to the hexagonal one.

We note that the relaxation simulations require very long times (from $0.5 \times 10^4 \mu\text{s}$ in regular cases up to $10^7 \mu\text{s}$ in the longest cases), indicating the difficulty to achieve the delicate balance between the two interactions to reach equilibrium. Energy minimization would improve radically if simple relaxation was replaced by a better algorithm such as the conjugate gradients [19] or the fire algorithm [20].

Regarding the best suited value of initial annealing temperature T_{start} reported in Table 2, we make numerous attempts to determine which value is the optimal one. The conclusion we draw is that the T -value should be high enough

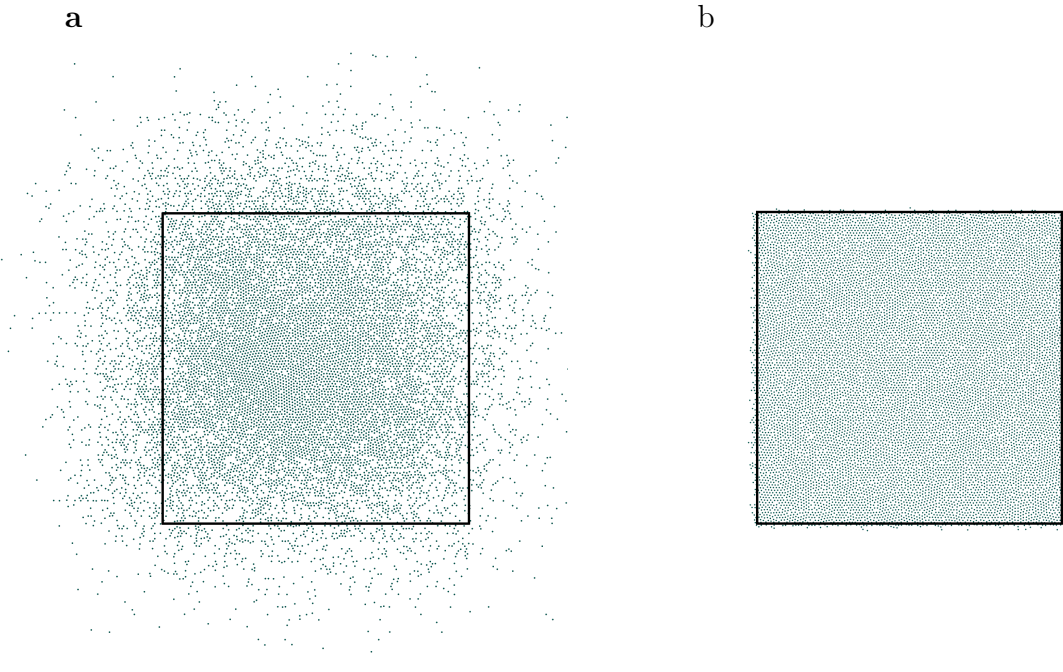


Figure 3: Snapshots of the final configurations of two annealing simulations, illustrating the particle diffusion across the PBC at two different values of T_{start} , for the same corrugation parameters ($a_{pot} = 8.8 \mu m$ and $V_0 = 1 zJ$) and simulation duration ($t \simeq 1.5 \times 10^4 \mu s$). **(a)** $T_{start} = 10 zJ$ and **(b)** $T_{start} = 1 zJ$.

to allow particles to explore a fair number of configurations, but not too high, to prevent the diffusion of particles across the PBC: we recall that a quasi-periodic external potential does not fit any PBC at all. The diffusion across the borders may introduce artefacts, namely particles experiencing a local corrugation environment contradicting that of formally neighbouring ones. Fig. 3 illustrates diffusion across the PBC during the annealing cycle.

The practical result of these considerations is that we use a T_{start} (in zJ) of the same order of magnitude as the considered V_0 (or even $T_{start} \ll V_0$, especially with $V_0 \ll 1 zJ$).

For each external potential spacing (a_{pot}), we generate the minimum-energy state for several amplitudes, in a range from $V_0 = 0.05 zJ$ up to $V_0 = 1000 zJ$, in order to explore our system possibilities. Eventually we find that the states with $V_0 \geq 10 zJ$ hold the same overall characteristics, thus we focus on a subset of corrugations $0.05 \leq V_0 \leq 10 zJ$, which cover the relevant features of this model.

3.2 Dynamic Simulations

When applying a \mathbf{x} -directed driving force, it is necessary to do so within a clear target range. This range depends on the corrugation amplitude, because it takes larger forces to overcome large corrugations. In previous work [3] based on a periodic potential, the static friction threshold of an isolated particle F_{1s} was introduced to set this scale. F_{1s} is the substrate maximum slope in the \mathbf{x} -direction, and it is clearly defined and easy to calculate in periodic geometry. Here we need to introduce properly F_{1s} even in quasiperiodic geometry. Clearly, out of dimensional arguments F_{1s} depends on V_0 and a_{pot} according to:

$$F_{1s} = \alpha \frac{V_0}{a_{pot}}, \quad (9)$$

where α is an dimensionless constant. Here we decide to define F_{1s} as the static friction threshold of a single colloidal particle sitting in the potential well at the origin, i.e. the “threshold” driving force needed to overcome the first potential barrier and to permit the single-particle to slide along the \mathbf{x} -axis. In order to have an idea of the relative strength of a particular driving force, its value is conveniently compared with the F_{1s} value appropriate for the given V_0 and a_{pot} . We compute α directly simulating a one-particle depinning transition, obtaining $\alpha = 4.279396 \pm 0.000001$ and we verified the consistence of the definition by changing a_{pot} and V_0 and obtaining a compatible α .

Different relaxed configurations associated to various substrate potential amplitudes V_0 show very different typical scales for forces and mean sliding velocities. To be able to compare the results of the dynamic simulations for different corrugations investigated, it is convenient to normalize forces and velocities suitably. For the forces, we express them in units of F_{1s} . For a global view of our system motion, we evaluate the center-of-mass velocity of the system (v_{cm}). Rather than velocities itself, one obtains better comparisons in terms of the average mobility

$$\mu = \frac{\langle v_{cm} \rangle}{F}. \quad (10)$$

For the free system ($V_0 = 0$), this mobility is determined by the viscous term to $(m\eta)^{-1}$, so it is convenient to report the dimensionless reduced mobility $\mu \cdot m\eta$, which equals unity in the $F \gg F_{1s}$ limit where the corrugation becomes almost irrelevant.

Starting from the best relaxed configuration for each set of parameters, we initially run a few quick simulations to catch a rough idea of the behaviour of the model: we discover that at low forces ($F \ll F_{1s}$) the majority of our states seems pinned. In particular, all the states characterized by a corrugation amplitude

$V_0 > 1$ zJ turn out well pinned up to a sizeable static friction threshold F_s , exhibiting quite similar overall features. We then focus our attention on the region between $V_0 = 0.1$ zJ and $V_0 = 1$ zJ, executing much longer simulations in this parameter range, starting from each equilibrium state and increasing the driving force F adiabatically in tiny steps of $\approx 0.01\% F_{1s}$, with each simulation starting from the end point of the previous one. These careful adiabatic changes in F allow us to minimize the dynamic effects which could be triggered by the sudden application of a large incremental force step. At each F increment we drop an initial portion (from the 50 to even 90%)² of the simulation, representing the initial transient response, and evaluate $\langle v_{cm} \rangle$ over the remaining part. We then sum up the dynamic response in graphs, representing the dimensionless relative mobility $\mu \cdot m\eta$ plotted against F/F_{1s} .

4 Static Equilibrium Properties

For each set of model parameters (a_{pot} and V_0), we select the best (i.e. lowest-energy) configuration obtained, and characterize it as follows.

4.1 Local Properties

To give an idea of the structural configurations after the annealing process, we report a few final configurations for different corrugation amplitudes in Fig. 4 and Fig. 5.

Regardless of the external potential characteristic spacing, in the states of small corrugation amplitudes ($V_0 \leq 0.1$ zJ) we identify an almost perfect triangular lattice, meaning that the corrugation strength is still not sufficient to visibly deform the monolayer. As the corrugation amplitude is increased a quite different colloidal disposition emerges, with the appearance of typical quasiperiodic patterns such as pentagons and flower-like motifs.

Due to a lower density of wells in the case of $a_{pot} = 8.8$ μm , the states of Fig. 4 are characterized by a more ordered appearance, especially with large V_0 , compared to Fig. 5, where for $a_{pot} = 5$ μm fewer wells are occupied by colloids, resulting in an apparent randomization.

These qualitative observations can be substantiated in quantitative histograms of the local potential energy, reported in Fig. 6 and Fig. 7. The color

²We drop the initial 50% of the simulation in the regular cases, when the system approaches a proper steady state within the simulation duration. For few delicate cases, such as the small corrugation ones, we drop up to 90% of the simulation, since the mean velocity of the system stabilizes only in the last part of extremely long simulations.

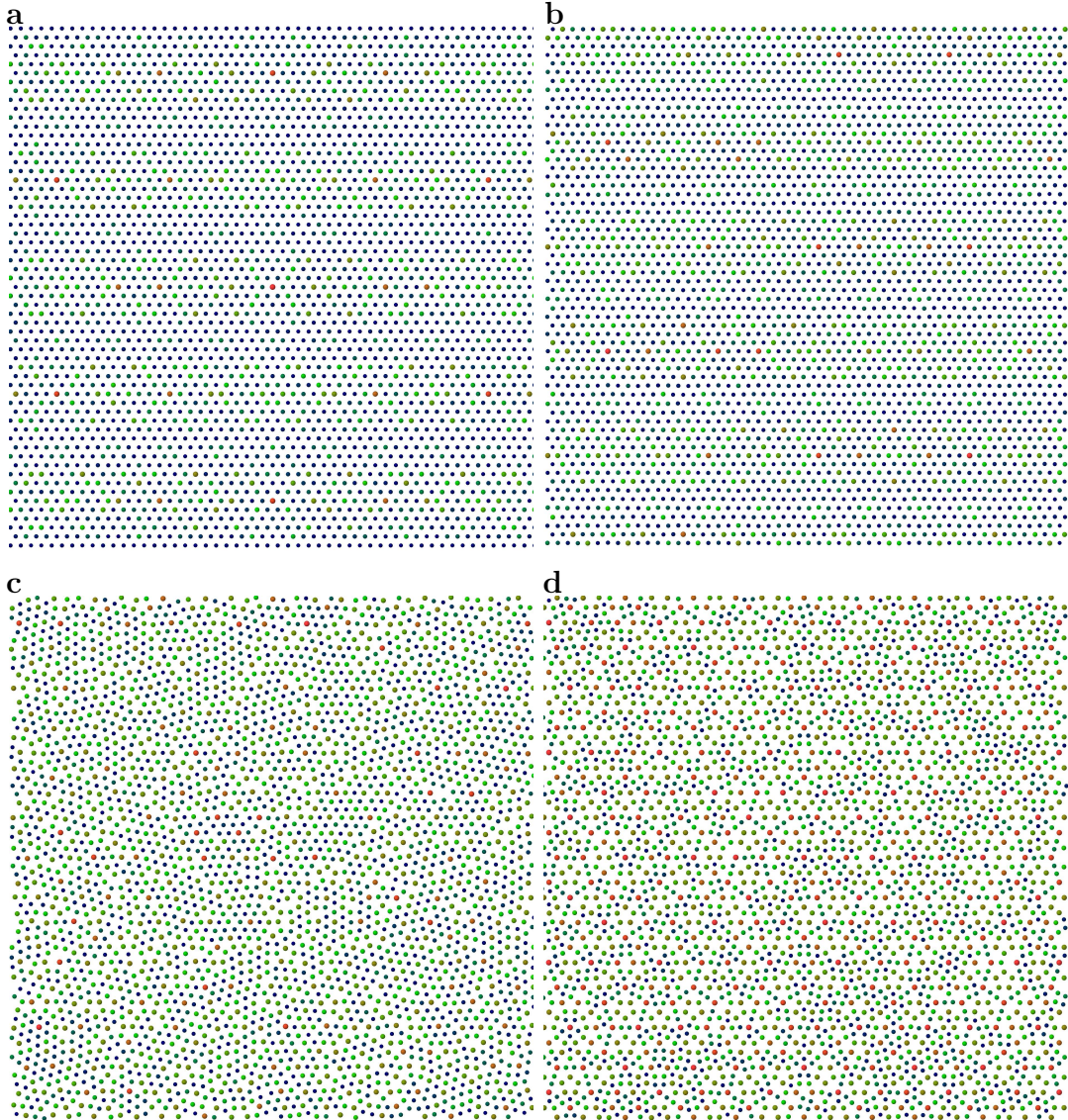


Figure 4: A central region of the relaxed configurations of the colloids interacting with the quasicrystalline potential with characteristic spacing $a_{pot} = 8.8 \mu\text{m}$ and amplitude (a) $V_0 = 0 \text{ zJ}$, (b) $V_0 = 0.1 \text{ zJ}$, (c) $V_0 = 1 \text{ zJ}$, (d) $V_0 = 50 \text{ zJ}$. Observe how the colloidal lattice transforms from a purely triangular lattice to a quasiperiodic-like pattern, characterized by the presence of a pentagonal structures typical of the five-fold-symmetric substrate potential. Colloidal particles are coloured by their local potential energy $W_5(\mathbf{r}_i)$: in an energy ascending order, from red (particles at or very close to deep potential minima), brown, dark-green, light-green to finally blue (particles at or very close to potential maxima). Colours correspond to those of Fig. 6.

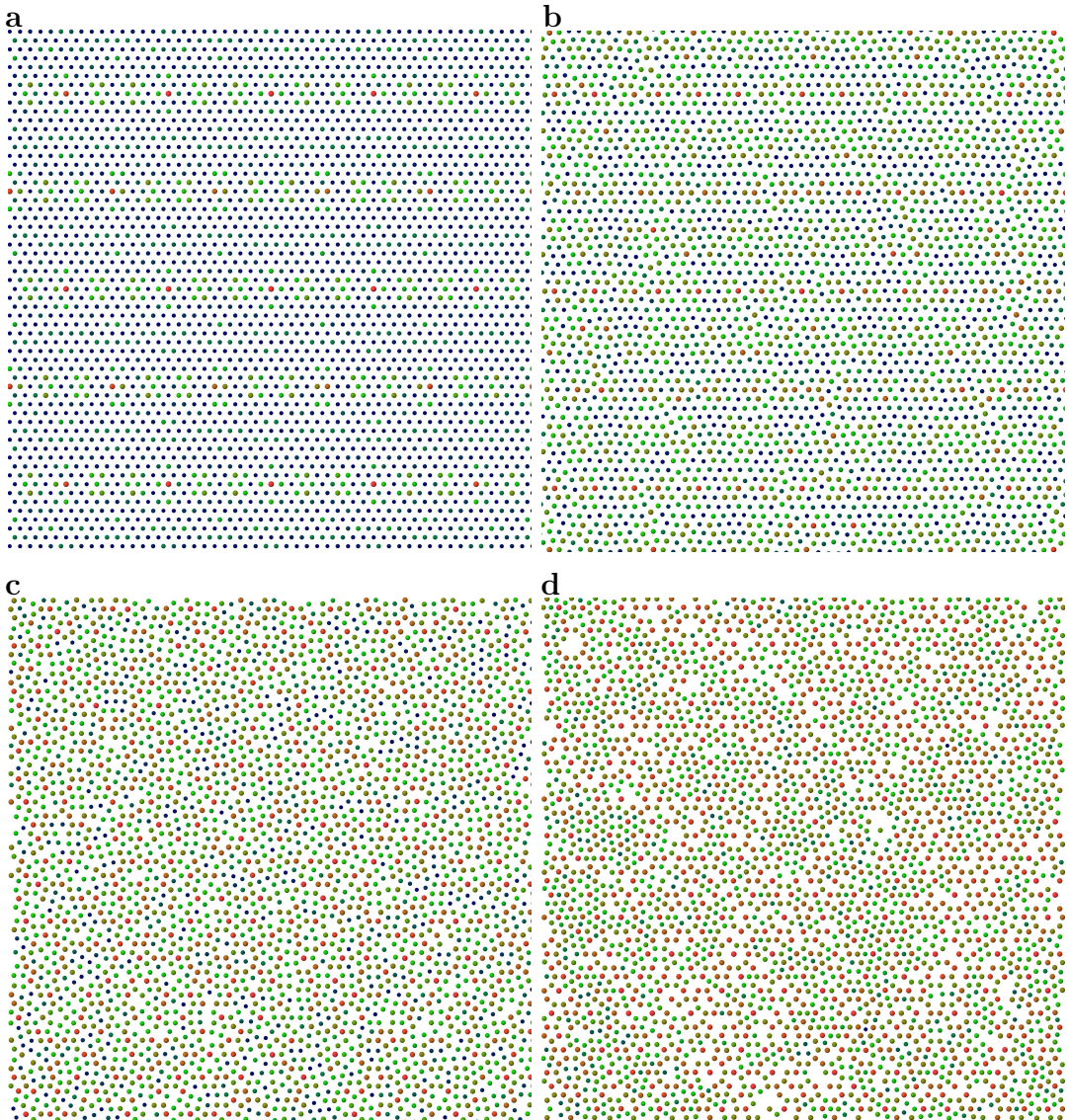


Figure 5: Same as Fig. 4 for the underdense case $a_{pot} = 5 \mu\text{m}$ and amplitude (a) $V_0 = 0.1 \text{ zJ}$, (b) $V_0 = 0.2 \text{ zJ}$, (c) $V_0 = 1 \text{ zJ}$, (d) $V_0 = 50 \text{ zJ}$. Compared to the overdense case, being here the particle density significantly lower than that of the minima, certain pentagonal structures are not significantly visible due to wells left empty (missing particles). Fewer (blue) particles sitting at maxima are visible for large V_0 .

coding of the colloids in these figures follows the local value of $W_5(\mathbf{r}_i)$, with red particles sitting at the deepest minima and blue particles near the highest maxima. Clearly, for the same V_0 , $a_{pot} = 5 \mu\text{m}$ allows for a better localization (fewer blue particles) than $a_{pot} = 8.8 \mu\text{m}$ with numerous blue particles even for the largest V_0 . One may be surprised to find that even for the largest corrugation

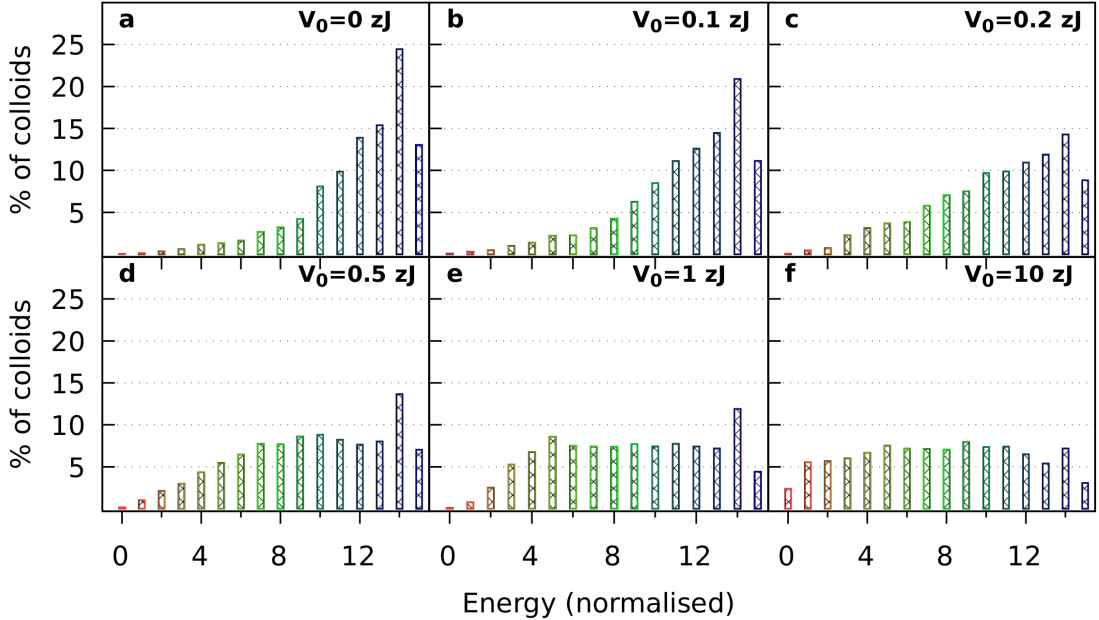


Figure 6: The distribution of local potential energy $W_5(\mathbf{r}_i)$ of the colloidal particles in their best relaxed configuration for the overdense case, $a_{pot} = 8.8 \mu\text{m}$. The energy, reported along the horizontal axis, is binned into 16 equal intervals between the minimum -1 (the 0th bin) of W_5 and its maximum 0 (the 15th bin). To avoid cross-boundary effects, for this static analysis we discarded an external slice of the supercell, reducing this statistics to a central square of side $500 \mu\text{m}$ containing approximately 8000 particles. Observe the evolution of this distribution from the crystalline state (a) ($V_0 = 0 \text{ zJ}$) toward increasing corrugations. Colours correspond to those of the particles in Fig. 4 .

relatively few particles end up in the deepest wells, but the reason for this is the relative scarcity of these "red-coloured" optimal points in the quasicrystalline landscape of Fig. 1 [21].

We also analyse the coordination number, i.e. the number of nearest neighbours of each colloid in the supercell [16]. The resulting histograms are shown in Fig. 8 and Fig. 9. When the corrugation potential is small ($V_0 < 1 \text{ zJ}$) the coordination number tends to remain identical to that of an hexagonal lattice: $n_{coord} = 6$. When V_0 is increased the number of nearest neighbours varies and spreads out into a distribution, approaching the tendency of having on average $n_{coord} = 5$ as we expect from a five-fold symmetry external potential.

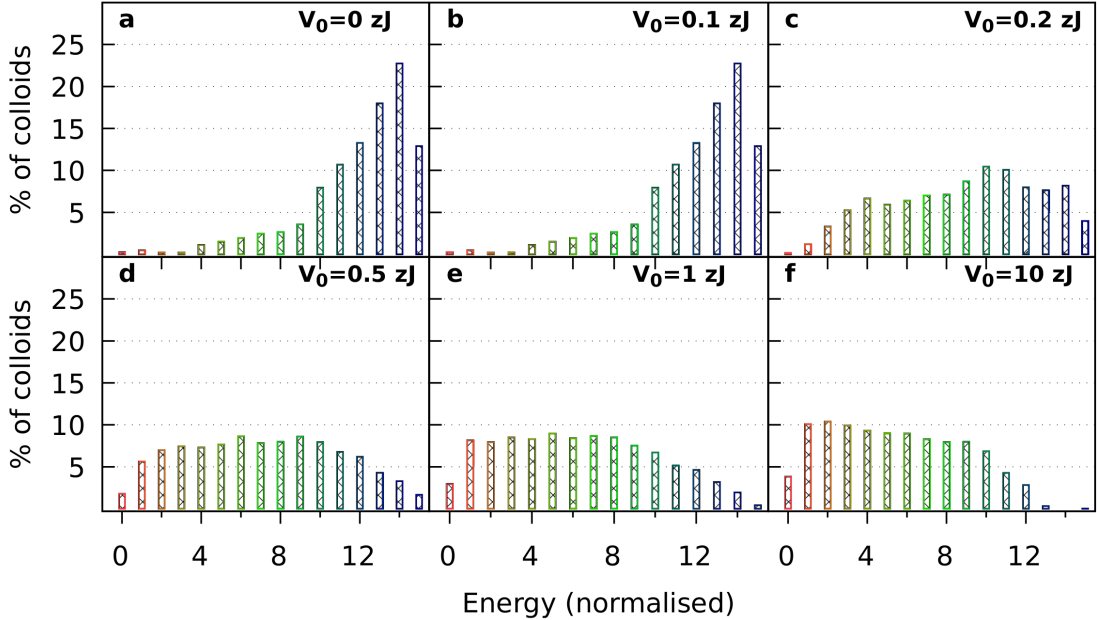


Figure 7: Same as Fig. 6, but for $a_{pot} = 5 \mu\text{m}$. In this underdense case for increasing corrugations more maxima are left unpopulated. Thus (as expected) we observe a slightly different distribution, shifted toward low-energy zone (if compared to Fig. 6).

4.2 Global Structural Properties

For a deeper, global, insight in the static structural properties of our relaxed configurations we examine the structure factor³

$$S(q) = \frac{1}{N^2} \left| \sum_{j=1}^N e^{-i\mathbf{q} \cdot \mathbf{r}_j} \right|^2. \quad (11)$$

We evaluate $S(\mathbf{q})$ following the protocol discussed in Section 3.4 of Ref. [16]. The resulting patterns help us to investigate and recognize long-range correlations in our colloidal system. In particular, as shown in Fig. 10 for both a_{pot} values we can distinguish two competing long-range orders: a triangular correlation for zero or small corrugation amplitude ($V_0 \ll 1 \text{ zJ}$), and a clear and characteristic decagonal structure when $V_0 \gg 1 \text{ zJ}$.

All the static-analysis tools agree with the following conclusion: if the corrugation amplitude is small (in our case, say $V_0 < 1 \text{ zJ}$), energy minimization

³The “standard” definition of the structure factor has a pre-factor of $\frac{1}{N}$ instead of our $\frac{1}{N^2}$, We prefer our definition that makes $S(\mathbf{q})$ normalised to unity for $\mathbf{q} = \mathbf{0}$.

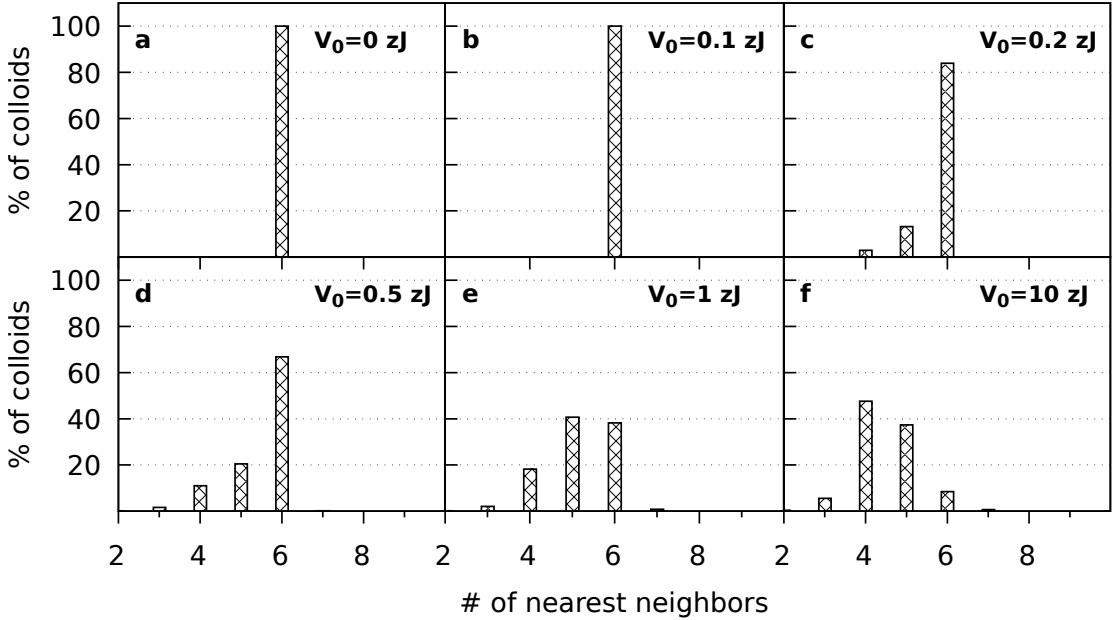


Figure 8: Histograms of the number of nearest neighbours, i.e. the coordination number for the overdense case $a_{pot} = 8.8 \mu\text{m}$. Note the evolution from the free state (**a**) with $n_{coord} = 6$, as expected for a perfect triangular lattice, to (**f**) large $V_0 = 10 \text{ zJ}$ where the number of nearest neighbours is more distributed (between 3 and 7), with a significant value at $n = 5$, reflecting the coordination number expected for a five-fold symmetry potential. This measures how an increasing corrugation amplitude V_0 deforms the colloidal lattice trying to adapt to its quasiperiodic shape. We will see consequences of this observation in the structure factors (see Sect. 4.2 and Sect. 5.3) and in the dynamic analysis.

substantially preserves the hexagonal geometry, with the inter-particle repulsion still playing a dominant role; whereas as V_0 is larger, the substrate potential energy dominates.

We initially assumed that we could associate the Aubry transition to this structural transformation of the static configuration of the monolayers while increasing the corrugation V_0 . However, this hypothesis is not confirmed by our dynamic analysis, as we will show in the next section.

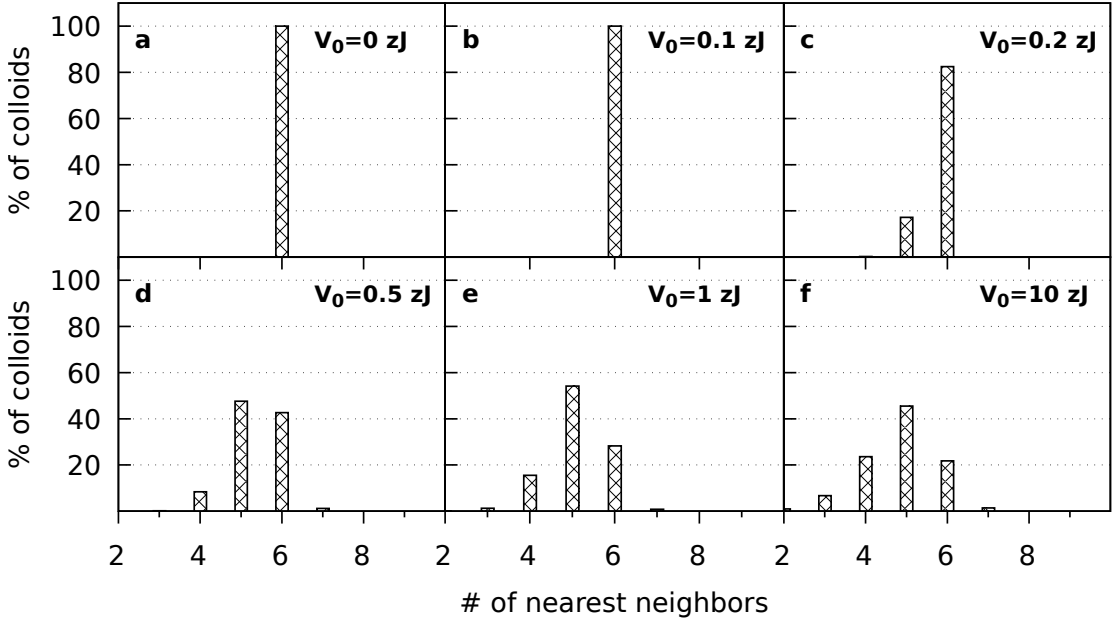


Figure 9: Same as Fig. 8, but for the underdense case ($a_{pot} = 5 \mu\text{m}$). Note the even larger percentage of colloids at $n = 5$ for large V_0 , indicating that the lower relative density allows the colloids to better fit the quasiperiodic five-fold local symmetry.

5 Dynamic Properties

Our goal in this section is to probe the system depinning and sliding by applying a constant driving force F to each colloid, thus driving the system away from its equilibrium state. It should reach a steady state (either advancing or immobile) in a reasonably short time, thanks to the overdamped dynamics.

As described in Sect. 3, in our simulations we increase the force step by step, at each step dropping an initial transient time ranging from the 50 to even 90% of the entire simulation time, in order to compute steady-state properties.

Now we can also see the role of the dissipative term $m\eta\dot{\mathbf{r}}_i$ in the equation of motion (1): it denies the possibility for our system to gain a large (ideally infinite, if the simulation time is as well) kinetic energy from the driving force. In the steady state it provides all the friction necessary to dissipate the work done by the external force F .

In this section we will focus on two main investigations: a general study of the mobility starting from each equilibrium relaxed state we obtained in the static phase, and an attempt to recognize the depinning transitions for those states, in

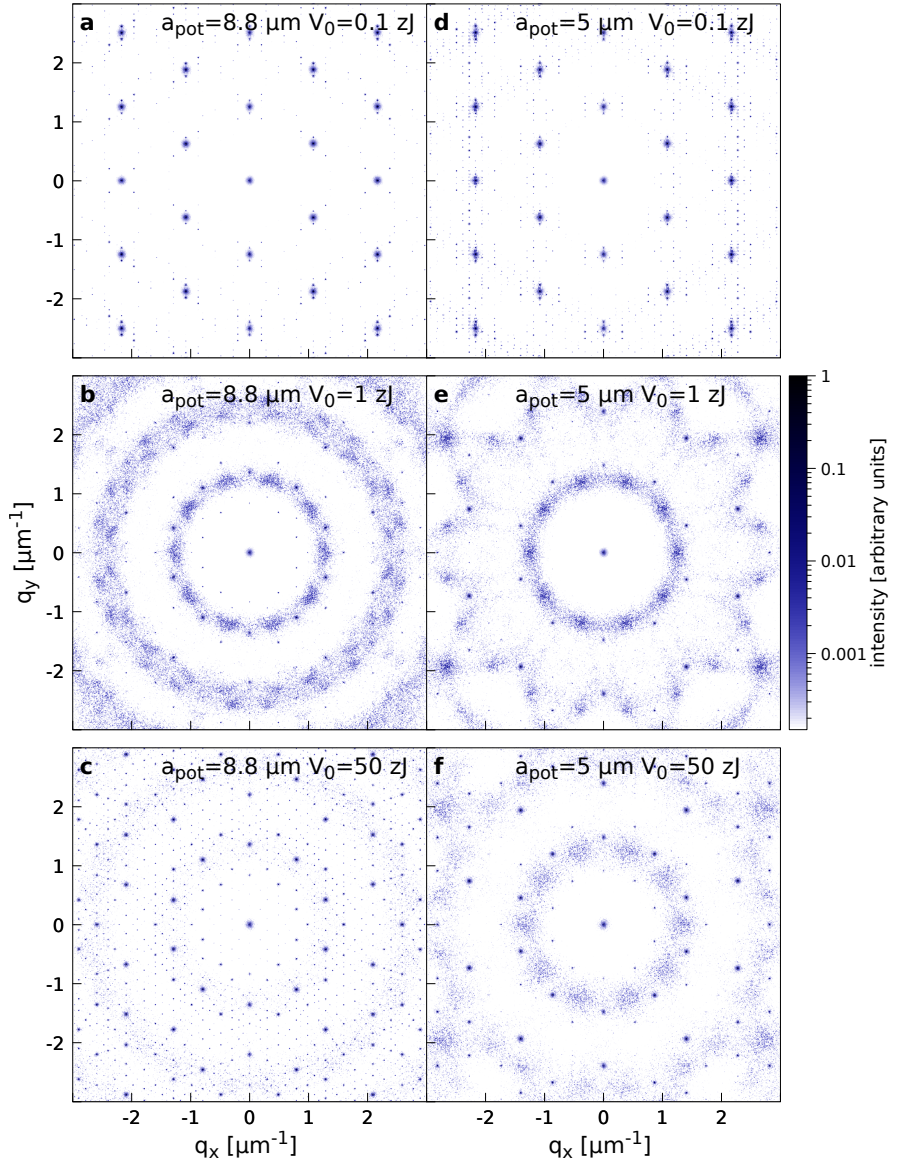


Figure 10: The evolution of the static structure factors of the relaxed states corresponding to both values of a_{pot} for increasing corrugation amplitude V_0 , as indicated in each panel. The transition between an essentially hexagonal structure, panels (a) and (d), to a decagonal one, panels (c) and (f), passes through intermediate and more “blurry” patterns (b) and (e), where the prevalent symmetry seems already decagonal.

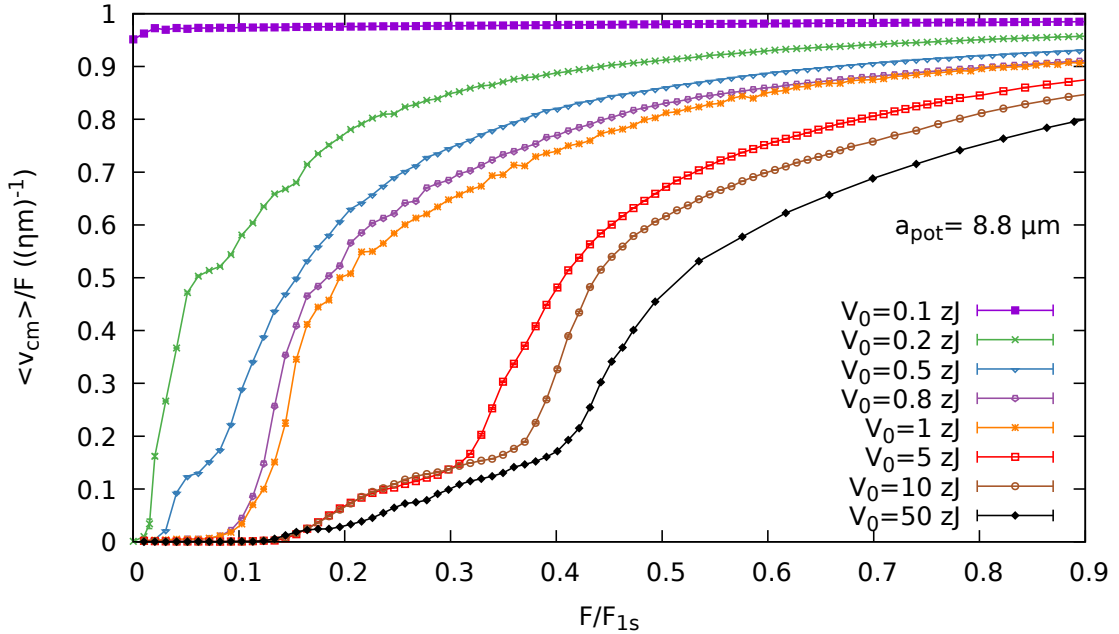


Figure 11: Mobility for $a_{pot} = 8.8 \mu\text{m}$, as a function of the normalized driving force for various values of V_0 indicated in the legend. Error bars are smaller than the points size. The state corresponding to $V_0 = 0.1 \text{ zJ}$ has a significantly larger mobility even down to the smallest forces that we could simulate, indicating a superlubric state. All other corrugations $V_0 \geq 0.2 \text{ zJ}$ produce pinned states instead.

order to identify a possible Aubry transition.

5.1 The Mobility

Following the protocol described in Sect. 3.2, we compute and report the normalized mobility as a function of the normalized driving force for sample values of the potential amplitude V_0 .

5.1.1 The Overdense Case $a_{pot} = 8.8 \mu\text{m}$

Figure 11 covers the overdense geometry, $a_{pot} = 8.8 \mu\text{m}$. From Fig. 11 lots of information can be extracted: first of all, note that for $a_{pot} = 8.8 \mu\text{m}$ there is a qualitative difference between the corrugation $V_0 = 0.1 \text{ zJ}$, whose associated mobility is systematically nonzero even down to the smallest forces, and all larger $V_0 \geq 0.2 \text{ zJ}$, whose mobility vanishes at nonzero applied force. The $V_0 = 0.1 \text{ zJ}$ state is a clear example of superlubric state, with the monolayer sliding almost

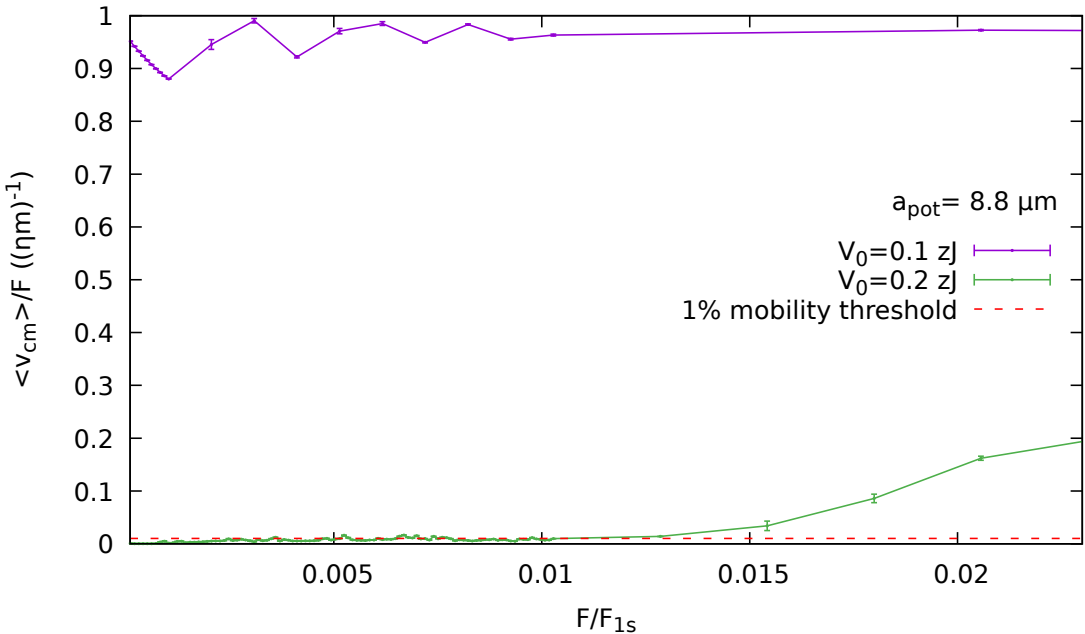


Figure 12: Same as Fig.11, zooming in to small forces ($0.001 < F/F_{1s} < 0.025$) the corrugations near the Aubry transition. The mobility fluctuations of the superlubric $V_0 = 0.1$ zJ curve are most likely the result of slightly inhomogeneous motion, with region of the layer being slowed differently by the substrate corrugation at different times and applied forces.

freely for applied forces as small as $0.01\% F_{1s}$, namely 4.86×10^{-6} fN for this case. Some residual pinning cannot be excluded for even smaller forces, but it may be an artefact of the finite system size, the periodic boundary conditions, or perhaps even of rounding errors in the integrations of the equations. In contrast, for all corrugation potential amplitudes $V_0 \geq 0.2$ zJ no free sliding occurs at small forces until a static-friction threshold F_s is exceeded: these states are pinned states.

Figure 12 zooms in the low-force region where these differences are quite evident. Since we label the $a_{pot} = 8.8$ μm $V_0 = 0.1$ zJ state as unpinned at even the smallest forces possible (i.e. superlubric), and $V_0 = 0.2$ zJ as pinned, the presence of the Aubry transition is recognized in this interval.

We note that for $V_0 \geq 5$ zJ the mobility curves exhibit a peculiar behaviour, with a sort of small-mobility step where the mobility increases quite slowly in the $0.2 \lesssim F/F_{1s} \lesssim 0.4$ region, followed by a sudden raise towards unity for $F/F_{1s} \gtrsim 0.4$, approaching the curves obtained for smaller V_0 . The explanation of such behaviour can be understood by examining the simulation trajectories



Figure 13: Intermediate snapshot relative to the simulation for $a_{pot} = 8.8 \mu\text{m}$ and $V_0 = 5 \text{ zJ}$ driven by an applied normalized force $F/F_{1s} \approx 0.25$, i.e. at the middle of the step-like region of the mobility curve in Fig. 11. The partial depinning is identified as resulting from the motion of horizontal channels highlighted by representing in bold red those particles whose displacement during the simulation of duration $\simeq 5 \times 10^4 \mu\text{s}$ exceeds one a_{pot} spacing. By comparison, if the reduced mobility $m\eta \langle v_{cm} \rangle / F$ was unity, over the same time interval, the displacement would be $\simeq 2a_{pot}$.

reported in Fig. 13 coloured in such a way to highlight the horizontal bands which advance, with the rest of the colloids remaining essentially immobile and not contributing to the mean velocity.

Localized motions of different kind are observed when investigating the low-mobility motions at very small forces, in a force-value region where no clear depinning is appeared yet.

Ideally the mobility would be expected to increase smoothly with the applied force with no oscillations or fluctuations. However Fig. 14 shows unexpected nonmonotonic fluctuations of the mobility, in particular for $V_0 = 0.2 \text{ zJ}$. Here, the

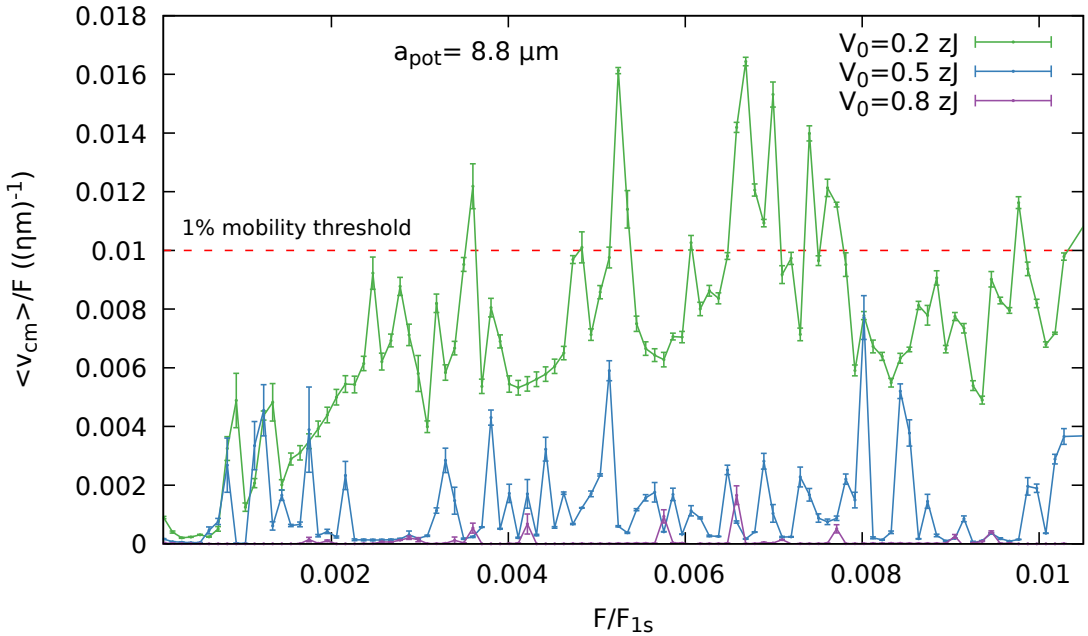


Figure 14: Mobility at small forces ($F \approx 0.0001 \div 0.01 F_{1s}$) for the first 3 pinned configurations of the overdense case: this zoomed portion of Fig. 11 shows unexpected fluctuations of the mobility, in particular for $V_0 = 0.2 \text{ zJ}$. In further analysis as in Fig. 15 we explain such fluctuations as symptoms of not long-enough simulations in those specific cases of small V_0 and small driving forces.

explanation of those fluctuations is the following: as the driving-force approaches the depinning threshold, local partial-depinning events take place, leading to a temporary increase of the mobility in certain cases. Such fluctuations are more related to the effective simulation time than to the specific force value, meaning that our already-long simulation time⁴ might be not long enough for such peculiar conditions of small corrugation amplitude and weak driving force. Fig. 15 substantiates these observations in a specific case.

5.1.2 The Underdense Case $a_{pot} = 5 \mu m$

As shown in Fig. 16, for this characteristic potential spacing the situation is similar: a superlubric state is recognized at $V_0 = 0.05zJ$ (free sliding down to $F \simeq 10^{-4} F_{1s} = 4.28 \times 10^{-6} \text{ fN}$), and all the other studied corrugations are pinned. Compared to the case of $a_{pot} = 8.8 \mu m$, where the superlubric character is found

⁴Ranging from 10^4 and $10^5 \mu s$, with some delicate simulations (for the smallest V_0) of duration up to $10^7 \mu s$.

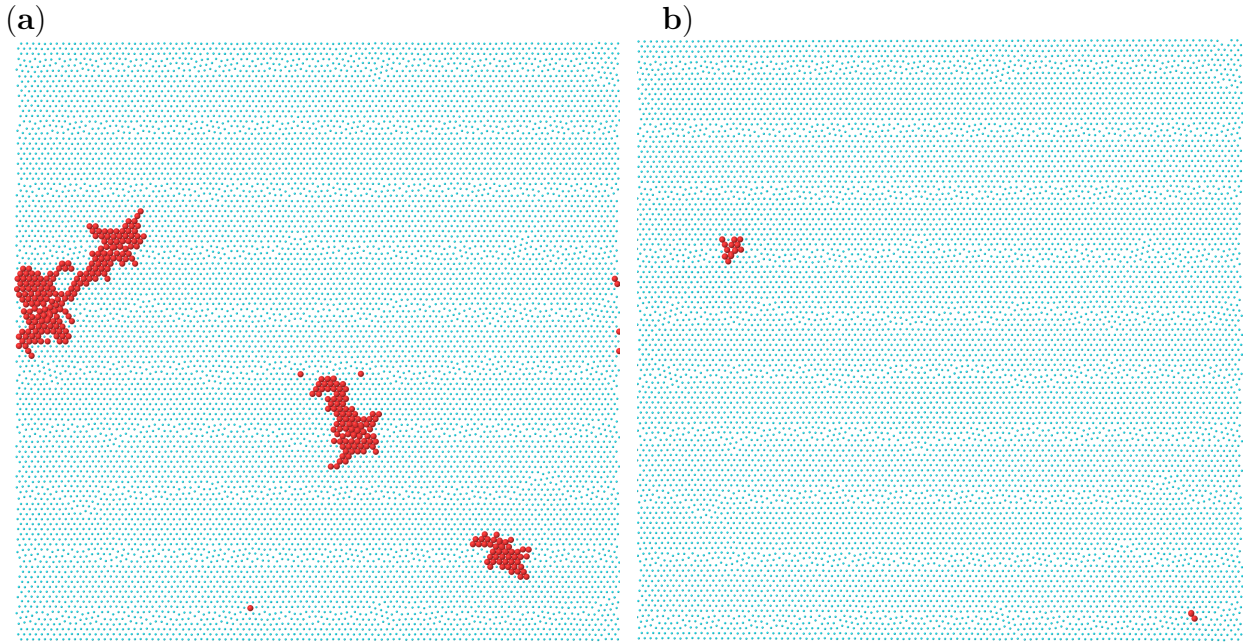


Figure 15: Snapshots relative to two successive force steps in simulations with $a_{pot} = 8.8 \mu\text{m}$ and $V_0 = 0.2 \text{ zJ}$. The partial depinning caused by the motion of few colloidal island is illustrated by highlighting in red those particles whose displacement during the simulation time (reduced to $5 \times 10^4 \mu\text{s}$ after the initial transient is dropped) exceeded $0.05 \mu\text{m}$. In panel (a) the driving-force is $F = 0.00095 \text{ fN}$, and clearly there are a few regions of the colloidal layer undergoing a partial depinning. Panel (b) shows the successive force step $F = 0.00096 \text{ fN}$, producing few smaller partial depinning. This suggests that the partial depinning of the colloidal monolayer might depend on the simulation time, rather than on the specific value of the forces: ideally, with much longer simulation times, the fluctuation in mobility values should not appear any longer. To confirm this hypothesis, we run a second simulation starting from the end-point of (a), without increasing the driving force (i.e. still applying a driving force $F = 0.00095 \text{ fN}$): the resulting displacements were almost identical to those of panel (b), proving the not-strict correlation between close force steps and partial depinning.

for $V_0 \leq 0.1zJ$, a smaller V_0 value associated to the superlubric configuration was expected, because a smaller a_{pot} produces steeper variations of $W_5(\mathbf{r})$, and, as a result, larger gradients, i.e. larger forces. Our estimation of the Aubry-type critical corrugation is therefore $0.05 \text{ zJ} < V_0^{Aubry} < 0.1 \text{ zJ}$, slightly smaller than for $a_{pot} = 8.8 \mu\text{m}$. To verify that the pinning of the $V_0 = 0.1 \text{ zJ}$ configuration

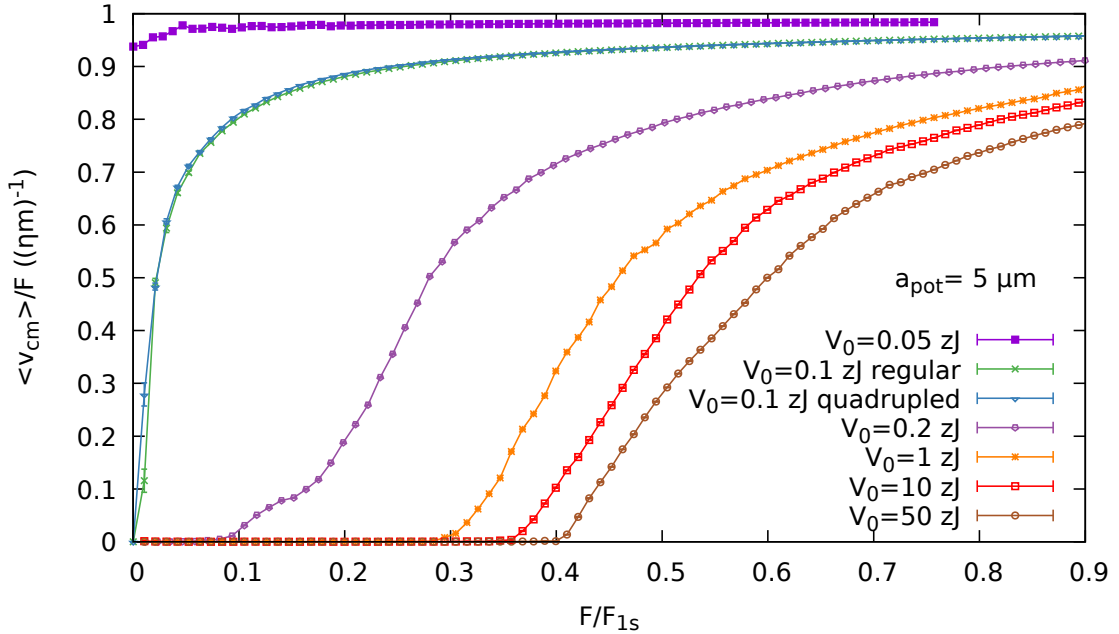


Figure 16: Same as Fig. 11 but for the underdense case $a_{pot} = 5 \mu\text{m}$. Differently from the overdense case, here the curve corresponding to $V_0 = 0.1 \text{ zJ}$ seems to tend to zero when the force decrease. For $V_0 = 0.05 \text{ zJ}$ we found a superlubric state. Clearly the other corrugations $V_0 \geq 0.2 \text{ zJ}$ are pinned states. Note that the dotted curve referred to in the legend as “quadrupled” corresponds to simulations carried out in a supercell with side doubled with respect to the regular one, thus containing four times as many colloids and presumably weaker boundary pinning, if any.

is not an artefact due to the imperfect boundary of the simulation supercell, we repeat the simulation for $a_{pot} = 5 \mu\text{m}$ and $V_0 = 0.1 \text{ zJ}$, but with a supercell with side doubled relative to the regular one (see Sect. 2.3), thus containing $N = 46400$ particles. The simulation results of such enlarged-size cell are quite the same as those of the “regular cell”, as shown by the almost perfectly overlapping curves of Fig. 16. We then exclude boundary effects, and label $V_0 = 0.1 \text{ zJ}$ state as certainly pinned, although with a very small static friction threshold.

We also note that for this lower wells occupation ratio there are no clear traces of partial sliding behaviour as in the curves in Fig. 11, due to the lower particle density not forcing any colloids near potential maxima where they are more likely to move, as occur for $a_{pot} = 8.8 \mu\text{m}$ case.

5.2 The Depinning Thresholds

In this subsection we focus in particular on the depinning, attempting to estimate the static-friction threshold for each investigated configuration of the system. To distinguish between an immobile configuration and one which is advancing under the effect of F , we establish two mobility thresholds: one corresponding to 1% of the free mobility, above which we actually observe a (often partial, in the overdense case) motion of the layer, and one corresponding to 4% of the free mobility, above which complete sliding typically occurs. For each curve of Fig. 11 and Fig. 16, we then fairly define two quantities: F_{creep} corresponding to the specific value of the driving force associated to crossing the 1% mobility threshold, namely the force above which the mobility exceeds 1% of the free mobility, and F_{depin} corresponding to a generally larger force associated to crossing the 4% mobility threshold. Fig. 17 reports these force thresholds for both values of a_{pot} , as a function of V_0 . This figure provides a sort of “dynamical phase diagram” with a statically pinned region below the 1% threshold (solid line), a sliding state above the 4% threshold (dashed line) and a creeping/undecided region in between. The smallest detected depinning thresholds are: for $a_{pot} = 8.8 \mu\text{m}$ and $V_0 = 0.2 \text{ zJ}$, $F_{depin} = 0.0154 \text{ fN}$; for $a_{pot} = 5 \mu\text{m}$ and $V_0 = 0.1 \text{ zJ}$, $F_{depin} = 0.0012 \text{ fN}$.

The region between the two curves for $a_{pot} = 8.8 \mu\text{m}$ is broader than for $a_{pot} = 5 \mu\text{m}$: this wider creep region is the result of the partial motion illustrated in Fig. 13, with no counterpart for $a_{pot} = 5 \mu\text{m}$.

5.3 Structural Properties

To verify if the transformation to the sliding state leads to significant structural rearrangement of the monolayer, we evaluate the structure factor (SF) in two specific conditions: the colloidal layer in “pre-depinning” and in “(full) sliding”.

For pre-depinning, we evaluate the SF for a snapshot of the colloidal layer driven by an applied force not-strong enough to induce sliding. Specifically, we adopt a value of F a few steps below the static-friction threshold, stressing the “incipient” character, i.e. the system being about to slide, if only the force would increase slightly. Fig. 18 reports the produced “pre-depinning” SF.

To obtain the “sliding” SF we use snapshots of the dynamically driven system, i.e. successive frames captured during the sliding. For a fairly global view of the structure during sliding, we obtain the reported SF by averaging⁵ over 10

⁵The difficulty of this approach is the great required amount of computational time: to obtain this average, the software is actually capturing serially 10 different SFs. With a sample containing ≈ 9000 particles after a circular cut, the total time required for evaluating $S(\mathbf{q})$ at 3.6×10^5 points on the \mathbf{q} grid is close to one month on one core of a 2.27 GHz Intel Xeon E5520.

frames picked up at regular time interval⁶, during which the system center of mass advances by a significant distance ($> a_{pot}$). Figs. 19-22 compare sliding SF for an applied driving force $F/F_{1s} \simeq 0.4$ and $F/F_{1s} \simeq 0.6$ to the static ones, in order to observe and highlight possible changes in structure for slower and faster driving.

The “pre-depinning” factors of Fig. 18 do not exhibit significant differences compared to the purely static ones. This is expected, since no actual sliding is occurring, and in practice no dramatic deformations of the lattice are observed, producing only variations in the Bragg peaks intensity.

The “sliding” factors are instead showing interesting features:

- for both a_{pot} , while sliding with an applied force $F \simeq 0.4F_{1s}$ in most cases no significant differences are observed, we only note minor intensity changes of the Bragg spots, with no rearrangements of particles and thus no significant change in geometry. In few cases significant differences are observed, such as the Bragg-spots broadening in Fig. 19 panel (e) and Bragg-spots splitting in Fig. 21 panel (e).
- for large corrugation amplitude ($V_0 \gtrsim 1$ zJ), with an applied force $F \simeq 0.6F_{1s}$ the colloidal lattice rearranges its geometry from the pentagonal one induced by the external potential (in particular for $V_0 \gtrsim 0.5$ zJ), back to configurations resembling the original hexagonal lattice.

The discrepancy between the SF computed at $F/F_{1s} \simeq 0.4$ and $F/F_{1s} \simeq 0.6$ for $V_0 \gtrsim 1$ zJ can be explained by the following observation: while sliding at $F/F_{1s} \approx 0.4$, not far above the depinning threshold, due to the slower motion, the effect of the quasicrystalline corrugation reveals stronger compared to the case of $F/F_{1s} \simeq 0.6$, where the colloidal layer, because of its faster motion, experiences an x -averaged quasicrystalline potential, reducing its effective interaction strength. However in the underdense case pentagonal and decagonal structures resist more even in the “faster” sliding SF, indicating the more effective role of the quasicrystalline forces for this a_{pot} value, see Fig. 22.

6 Discussion and Conclusion

We have investigated static and frictional properties of a model for colloidal particles interacting with a quasicrystalline 2D corrugation profile.

For the statics, we obtain the following main results:

⁶The time interval between successive frames is related to the simulation time, which vary typically in the range $10^4 \div 10^5 \mu\text{s}$.

- In both the analysed relative densities, we find that for small corrugation amplitude ($V_0 = 0.1$ zJ) the initial hexagonal symmetry is retained, whereas when the potential amplitude is increased ($V_0 \gtrsim 0.5$ zJ) a quasicrystalline order emerges, becoming the dominant geometry in particular for $V_0 \gtrsim 1$ zJ.
- The distribution of local energy changes accordingly, as well as the main coordination number: in the overdense case ($a_{pot} = 8.8$ μm), with more particles than deep potential wells, the distribution of local corrugation energy is flat for $V_0 \gtrsim 0.5$ zJ, with a significant fraction of particles near the corrugation maxima even for large V_0 . In the underdense case ($a_{pot} = 5$ μm), as V_0 is increased the distribution shifts toward low local energy, and leaving the potential maxima practically unpopulated.
- In the same way, the coordination number evolves from the typical hexagonal $n = 6$ for the smallest potential amplitudes, approaching a distribution compatible with the five-fold symmetry underneath as V_0 increases, especially in the underdense case ($a_{pot} = 5$ μm).
- The analysis by means of static structure factor shows the evolution from hexagonal to decagonal/pentagonal patterns as the potential amplitude is increased.

Concerning the frictional dynamics, the following main conclusions can be drawn:

- For the overdense case ($a_{pot} = 8.8$ μm), we observe a superlubric state for $V_0 \leq 0.1$ zJ. Starting from $V_0 \geq 0.2$ zJ, all the configurations are pinned, characterized by a finite static friction. Thus, we can identify an Aubry-type transition between those corrugation amplitudes.
- For the underdense case, superlubric states are observed for $V_0 \leq 0.05$ zJ. For $V_0 \gtrsim 0.1$ zJ all the configurations are pinned. We then locate the Aubry-type transition between those corrugation amplitudes.
- Due to spatial inhomogeneity of the substrate potential landscape, it is not trivial to identify a sharp depinning force, especially in the overdense case. We compare the trends of the minimum force F needed to reach two different mobility thresholds (1% and 4% of the free mobility). In the underdense case they yield substantially equivalent results, but in the overdense one significant deviations with an undecided slow-drift interval in between.

A more precise determination of the Aubry transition will require exploring in greater details the region around $V_0 = 0.1$ zJ for both corrugations.

The states characterized by inhomogeneous partial sliding at intermediate forces are peculiar of the quasicrystalline system and also deserve further examination.

The most important conclusion of the present work is that in the quasicrystalline geometry a structural transformation occurs far above the Aubry transition. Practically hexagonal-lattice states remain indeed weakly pinned across an entire range of moderate V_0 values. This conclusion is at complete variance with the result that in hexagonal symmetry the Aubry transition coincides with a first-order structural change [10].

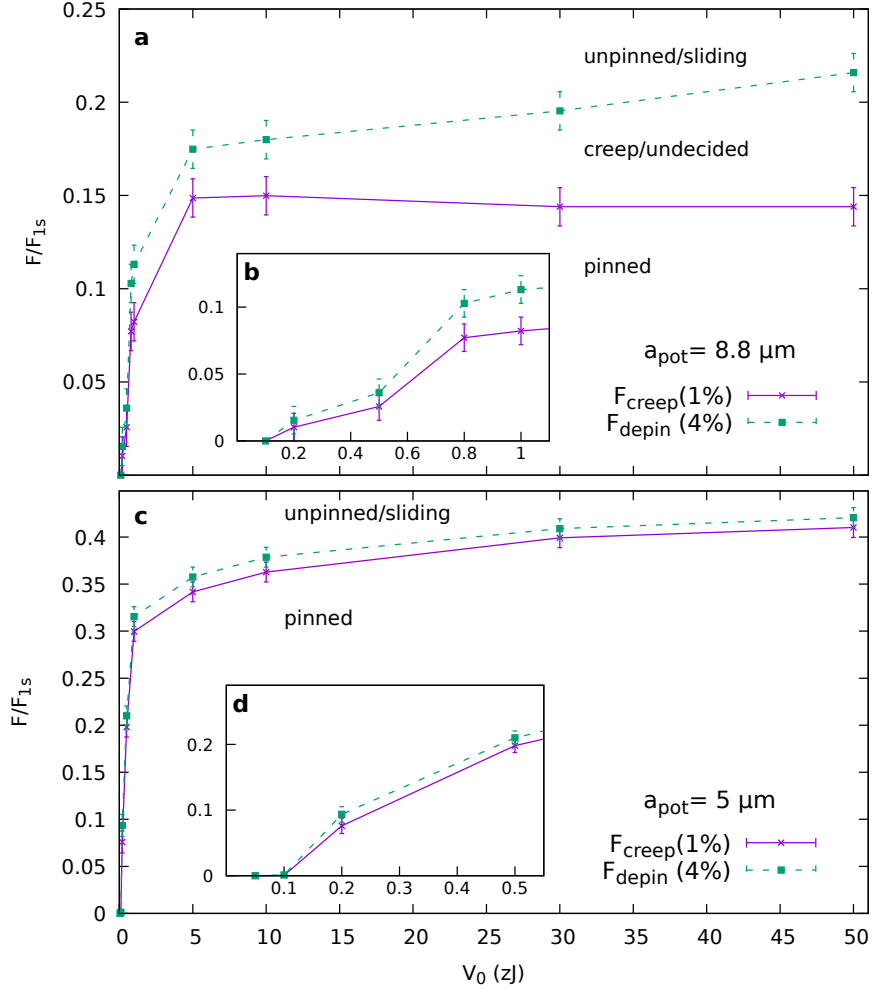


Figure 17: F_{creep} , the force value corresponding to crossing the 1% mobility threshold, and F_{depin} , the force values corresponding to crossing the 4% mobility threshold, as a function of the corrugation amplitude V_0 , for both a_{pot} values as indicated. Panels (b) and (d) zoom in the small V_0 region. Note that where $F_{depin} = F_{creep} = 0$ a superlubric state characterized by null static friction is observed. In panels (c), (d) F_{creep} and F_{depin} have tiny but nonzero values associated with $V_0 = 0.1$ zJ, being this state an example of an (extremely weakly) pinning. Instead for $V_0 = 0.05$ zJ $F_{depin} = F_{creep} = 0$ within our resolution.

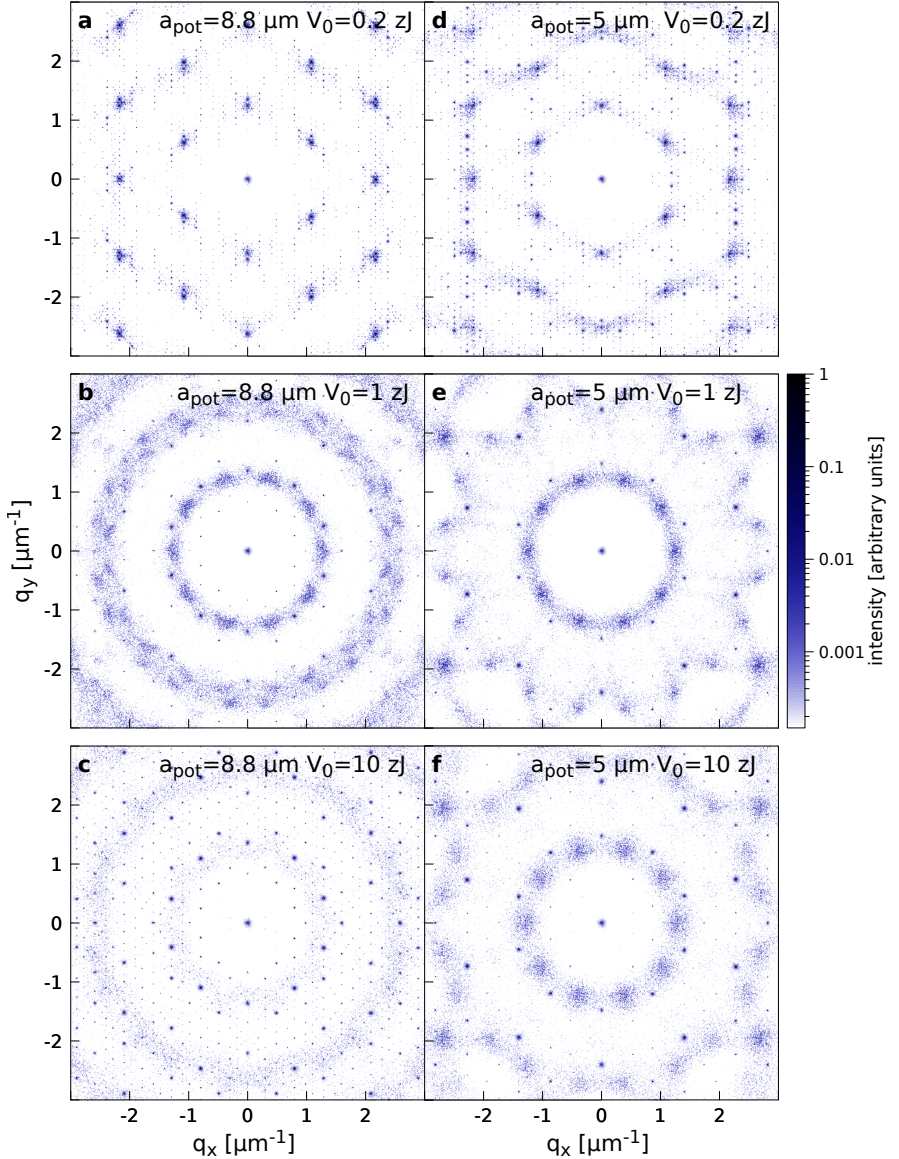


Figure 18: “Pre-depinning” structure factors evaluated for snapshots of the system with an applied force almost strong enough to induce sliding. Each panel indicates the corresponding value of a_{pot} and V_0 . The forces are: (a) $F = 6 \times 10^{-5}$ fN, (b) $F = 3.5 \times 10^{-2}$ fN, (c) $F = 0.6$ fN, (d) $F = 1.6 \times 10^{-4}$ fN, (e) $F = 4.5 \times 10^{-2}$ fN, (f) $F = 2.97$ fN. Compared to the static SF (shown in Fig. 19 (d), 20 (a) and 20 (d) for $a_{pot} = 8.8$ μm , and of Fig. 21 (d), 22 (a) and 22 (d) for $a_{pot} = 5$ μm), apart from relatively mild intensity and shape changes of the Bragg spots, no major differences arise.

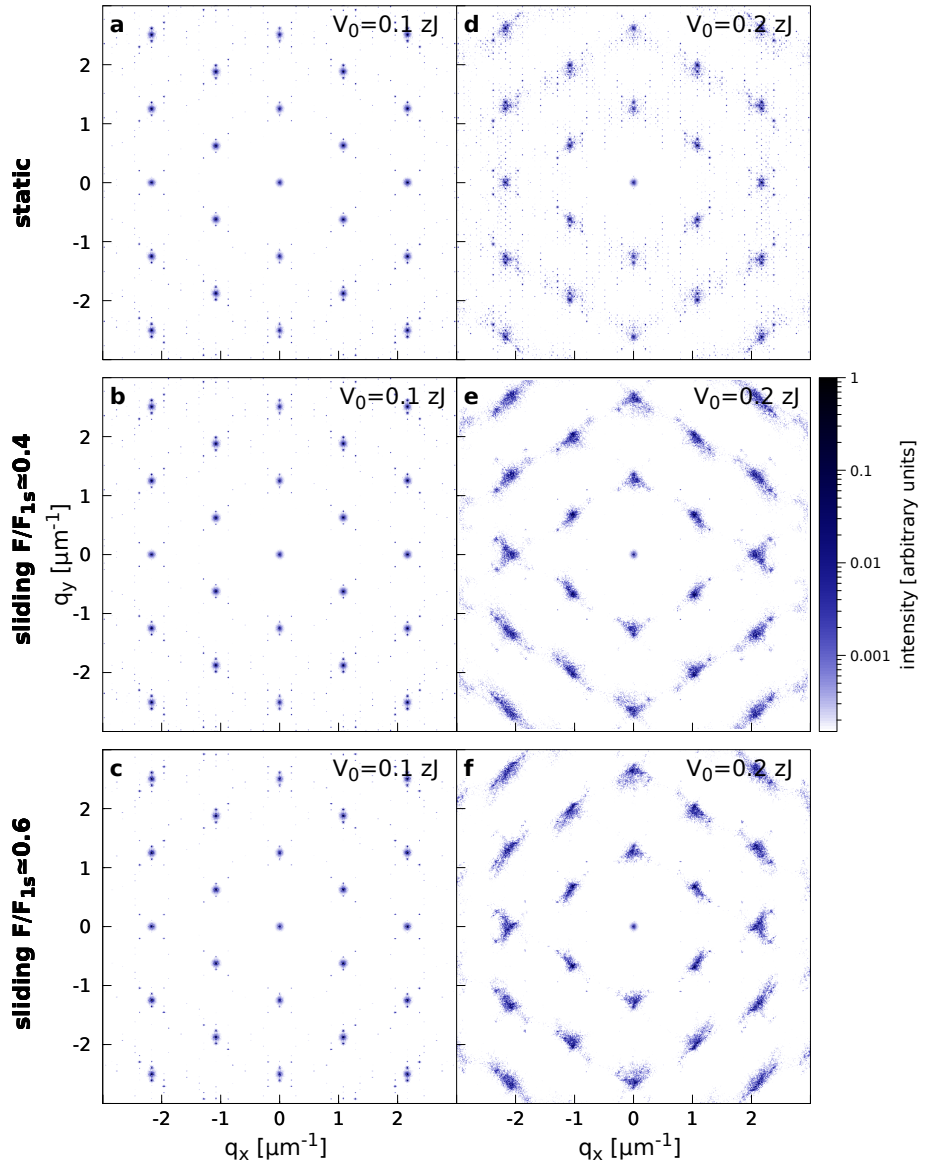


Figure 19: Comparison between static SF (panels **(a)** and **(d)**), “sliding phase” SF computed at $F/F_{1s} \approx 0.4$ (panels **(b)** and **(e)**) and at $F/F_{1s} \approx 0.6$ (panels **(c)** and **(f)**) for $a_{pot} = 8.8 \mu\text{m}$ and V_0 indicated in the panels. Compared to the static SF, tiny differences are observed in the intensity of Bragg peaks for $V_0 = 0.1 \text{ zJ}$. The sliding factors for $V_0 = 0.2 \text{ zJ}$ show instead broader intensity peaks, retaining an hexagonal but blurrier motif. For those small- V_0 configurations no geometry changes are observed.

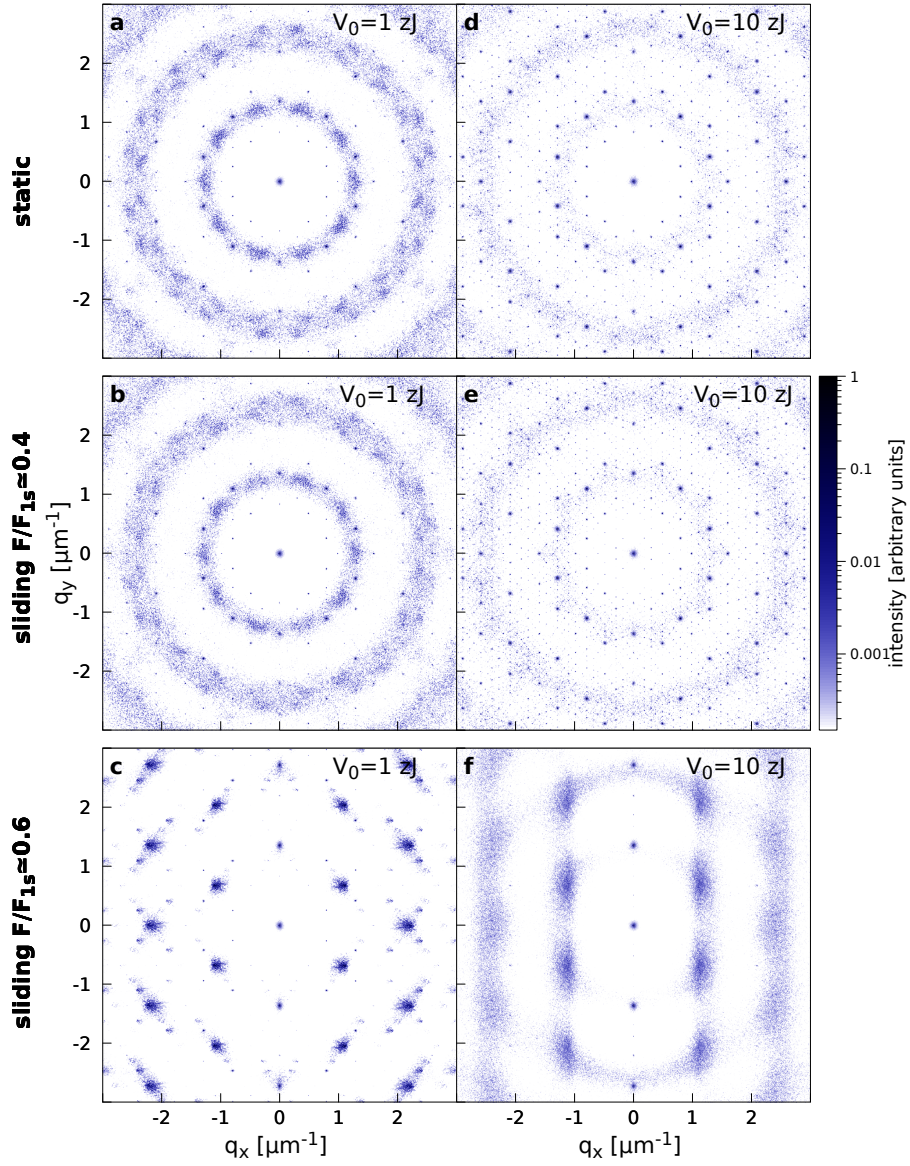


Figure 20: Same as Fig. 19, for $a_{pot} = 8.8 \mu\text{m}$ and V_0 indicated in figure. Compared to the static SF, tiny differences are observed in the intensity of the Bragg peaks in (b), (e), whereas evidences of important geometry changes are observed in (c), where the pentagonal structures characterizing the static states leave place to triangular structures. In panel (f) a clear motif does not emerge, indeed in real space this sliding state is characterized by an almost random mixture of structures.

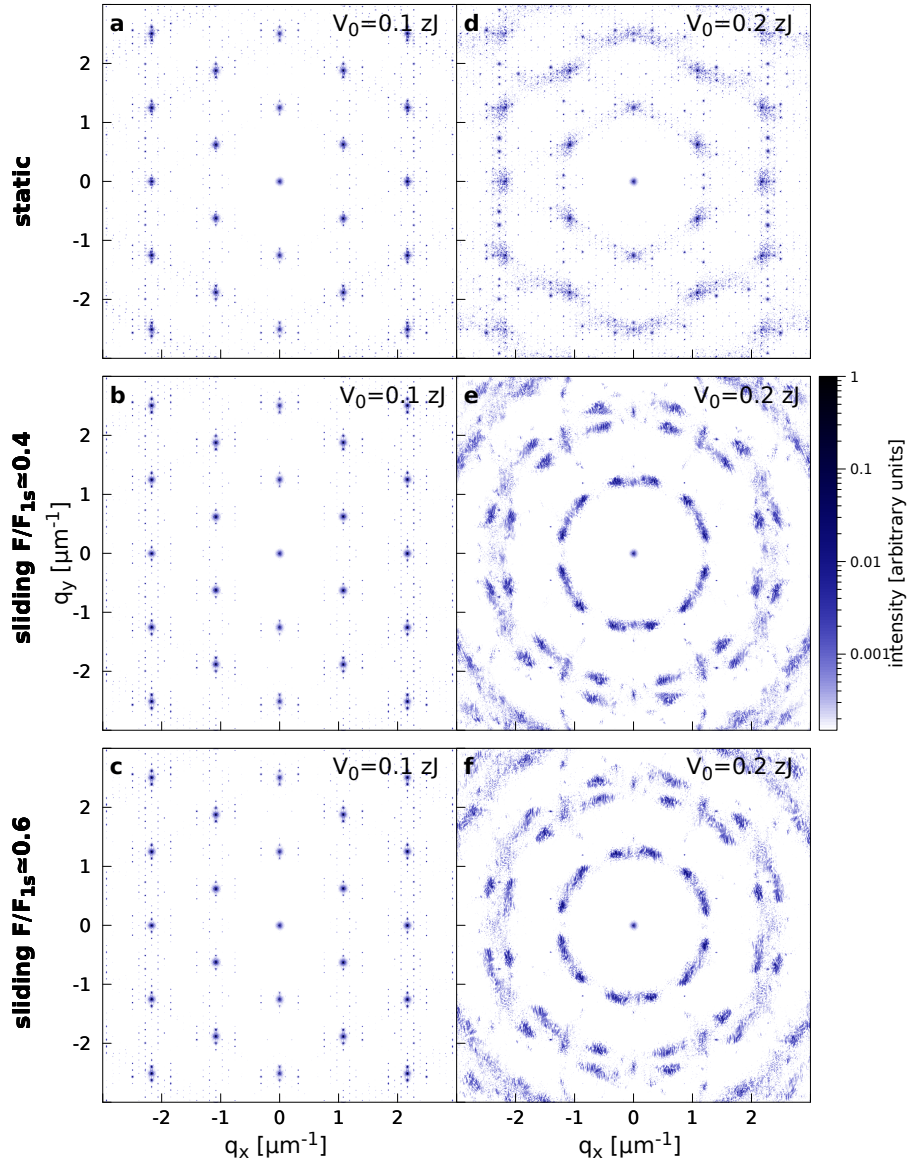


Figure 21: Same as Fig. 19, for $a_{pot} = 5 \mu\text{m}$ and V_0 indicated in figure. The state for $V_0 = 0.2 \text{ zJ}$ shows a peculiar interference pattern for both driving forces: in real space we observe at least two main regions with the same hexagonal symmetry but with different orientations, causing the spots splitting in panel (f).

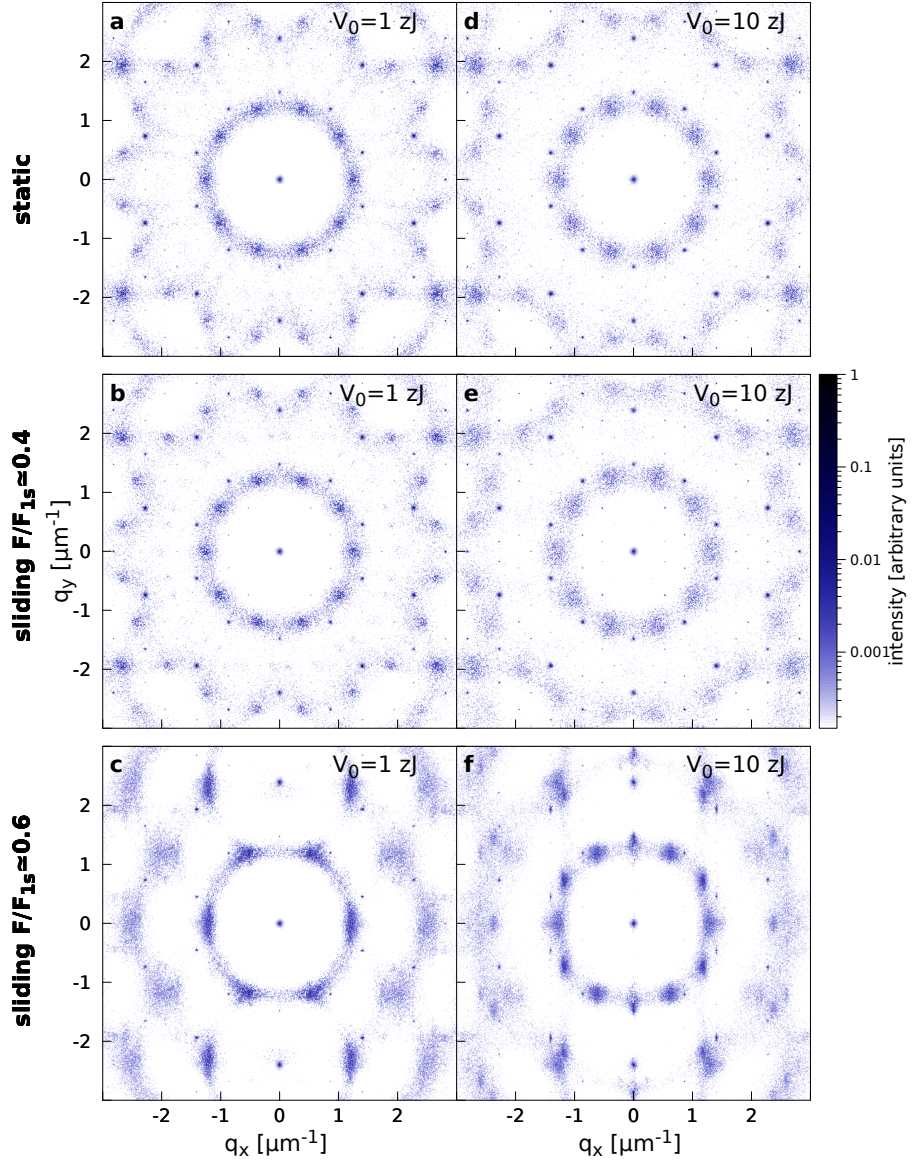


Figure 22: Same as Fig. 19, for $a_{pot} = 5 \mu\text{m}$ and V_0 indicated in the panels. Same considerations as in Fig. 20 apply here. Note that the sliding SF at $F/F_{1s} \approx 0.6$ shows 30° -rotated hexagonal structures at $V_0 = 1 \text{ zJ}$, and dodecagonal structures at $V_0 = 10 \text{ zJ}$. In both these SFs, decagonal patterns also emerge.

References

- [1] A A Lepeshev et al 2016 IOP Conf. Ser.: Mater. Sci. Eng. **155**, 012014 (2016).
- [2] T. Bohlein, J. Mikhael, and C. Bechinger, Nat. Mater **11**, 126 (2012).
- [3] A. Vanossi, N. Manini, and E. Tosatti, P. Natl. Acad. Sci. USA **109**, 16492 (2012).
- [4] J. Mikhael, M. Schmiedeberg, S. Rausch, J. Roth, H. Stark, and C. Bechinger, P. Natl. Acad. Sci. USA **114**, 7214 (2010).
- [5] M. H. Müser and M. O. Robbins, Phys. Rev. B **61**, 2335 (2000).
- [6] S. Aubry and P.-Y. Le Daeron. Phys. D **8**, 381–422 (1983).
- [7] M. Peyrard and S. Aubry. J. Phys. C **16**, 1593 (1983).
- [8] Y. I. Frenkel and T. Kontorova. Zh. Eksp. Teor. Fiz. **8**, 1340 (1938).
- [9] D. Mandelli, A. Vanossi, M. Invernizzi, S.V. Paronuzzi Ticco, N. Manini, and E. Tosatti, Phys. Rev. B **92**, 134306 (2015).
- [10] T. Brazda, A. Silva, N. Manini, A. Vanossi, R. Guerra, E. Tosatti, and C. Bechinger, Phys. Rev. X **8**, 011050 (2018).
- [11] J.A. Kromer, M. Schmiedeberg, J. Roth, and H. Stark, Eur. Phys. J. E, **36**, 25 (2013).
- [12] J.A. Kromer, M. Schmiedeberg, J. Roth, and H. Stark, Phys. Rev. Lett. **108**, 218301 (2012).
- [13] J. Mikhael, J. Roth, L. Helden, and C. Bechinger, Nature **454**, 501 (2007).
- [14] M. Bellagente, *Sliding on a quasicrystal: a colloidal model*, Bachelor thesis, Università degli Studi di Milano, 2016. <http://materia.fisica.unimi.it/manini/theses/bellagente.pdf>.
- [15] D. Mandelli, A. Vanossi, N. Manini, and E. Tosatti. Phys. Rev. Lett. **114**, 108302 (2015).
- [16] A. Silva, *Simulation of the depinning transition in a 2D colloidal layer*, Master thesis, Università degli Studi di Milano, 2017. <http://materia.fisica.unimi.it/manini/theses/silva.pdf>.
- [17] M. Schmiedeberg and H. Stark, Phys. Rev. Lett. **101**, 218302 (2008).

- [18] L. M. Floría and J. J. Mazo, Adv. Phys. **45**, 505-598, (1996).
- [19] M.R. Hestenes and E. Stiefel, J. Res. Natl. Bureau Stands. **49**, 409 (1952).
- [20] E. Bitzek, P. Koskinen, F. Gahler, M. Moseler, and P. Gumbsch, Phys. Rev. Lett. **97**, 170201 (2006).
- [21] M. Colombo, *The structure of the minima of a quasiperiodic potential in 2D* Bachelor thesis, Università degli Studi di Milano, 2017. <http://materia.fisica.unimi.it/manini/theses/colombo.pdf>.